UNIVERSIDADE DE LISBOA
FACULDADE DE CIÊNCIAS
DEPARTAMENTO DE BIOLOGIA VEGETAL

Characterising the Formation and Functional Role of Vesicular Clustering during Influenza A Virus Infection

Ana Laura Vinagre Costa e Sousa

Mestrado em Microbiologia Aplicada

Dissertação orientada por:
Doutora Maria João Amorim
Professora Doutora Maria Filomena Trabucho Caeiro

2017

"Human life itself may be almost pure chaos, but the work of the artist is to take these handfuls of confusion and disparate things, things that seem to be irreconcilable, and put them together in a frame to give them some kind of shape and meaning" – Katherine Anne Porter

Acknowledgements

"Sometimes the most ordinary things could be made extraordinary, simply by doing them with the right people" – Elizabeth Green

I would like to first say thank-you to my "chefa", Erin Telley for opening the doors of the Electron Microscopy field to me and supporting my attendance at conferences and courses. Without a doubt, if I did not have established my career at *Instituto Gulbenkian de Ciência*, I would not have developed this work. Also, if I was not at *Instituto Gulbenkian de Ciência*, I would not have met my lab mate Sara. Some results described in this thesis were accomplished with her help and support by freezing her hands during several afternoons but also for cheering me up in the hard days – chocolate always make the days brighter - made this work undoubtedly easier. As well, I have to thank my lab colleagues, Joana and Marta, who helped me with the cryostat sections, and Luis, who helped me with the super-resolution acquisitions and reconstructions.

I would like to express my gratitude to my external supervisor, Doctor Maria João Amorim, for accepting me into her group – Cell Biology of Viral Infection (CBV). She gave me intellectual freedom in my work and engaged in me new ideas. To all in CBV group, thank-you for listening all the electron microscopy presentations. Also from the CBV group, I want to highlight all the support and the friendship from Silvia. Her help with experiments when my days were overwhelming but also with the patience necessary for reviewing my reports and thesis, always putting complex ideas into simple terms and demanding a high quality of work from which I greatly benefited as a student but also as a professional in science. I also need to emphasize the support to all the bureaucratic questions from my internal supervisor Professor Filomena Caeiro.

Finally, although this master degree was one of the hardest things I did, I cannot forget the friends that it brought into my life. First my car sharing colleague Alexandra. I cannot thank-you more for all the talks and the messages! Although you still doubt, I can tell you are a great friend and you have a big heart that you hide so well that only the ones that are persistent enough can have access to. But also my "montaditos" team: André, Bia e Jorge. You guys made my time at *Faculdade de Ciências* lot more fun.

To my family from the heart: Luis, Flávia, Abreu, Vanessa e Gonçalo. Saying sorry for not being present it's not enough. Last the most important person, my "mamy" which was, is and will be always present in the bad and in the good times.

Characterising the Formation and Functional Role of Vesicular Clustering during Influenza A Virus Infection

Ana Laura Vinagre Costa e Sousa

2017

This thesis was fully performed at *Instituto Gulbenkian de Ciência* under the direct supervision of Dr Maria João Amorim in the scope of the Master in Applied Microbiology of the Faculty of Sciences of the University of Lisbon.

Resumo

Os vírus Influenza, que pertencem à família *Orthomyxoviridae*, estão divididos em quatro tipos A, B, C e D (Hause et al. 2013; Hause et al. 2014). Entre estes, o influenza A (IAV) é o vírus que causa maior impacto na saúde pública. O seu reservatório natural são as aves marinhas, no entanto possui a capacidade de gerar infeções zoonóticas encontrando-se disseminado em muitas espécies de aves e mamíferos (Acheson 2011; Taubenberger & Kash 2010). Nos seres humanos, o IAV é o patógeno responsável pela gripe, uma doença aguda respiratória associada a alta morbidade e mortalidade (Lofgren et al. 2007).

O IAV é composto por um invólucro viral derivado da membrana plasmática da célula. Este envelope é revestido por uma camada externa de proteínas virais, designadamente hemaglutinina e neuraminidase. O interior do virião contém o genoma viral, constituído por oito complexos ribonucleoproteicos (vRNPs). Cada vRNP é composto por um dos oito segmentos de ácido ribonucleico viral que codificam para diferentes proteínas virais. Os vRNPs funcionam como unidades independentes sendo necessário um conjunto completo de oito vRNPs diferentes para a montagem de uma partícula infeciosa (Fields et al. 2007).

Os vRNPs são transportadas por *piggyback* em vesículas destinadas à periferia da célula através da interação entre a polimerase 2 viral e a GTPase *Ras related in brain* 11 (Rab11) (Amorim et al. 2011; Eisfeld et al. 2011; Momose et al. 2011). Em homeostasia, o Rab11 está envolvido na reciclagem de proteínas endocitadas. Regula a formação, movimento e fusão de vesículas originárias do compartimento de reciclagem de endossomas e encontra-se espalhado pelo citoplasma (Grant & Donaldson 2009). Em células infetadas, o Rab11 acumula no citoplasma formando agregados vesiculares. Sabe-se que estas vesículas são heterogéneas, compostas por membrana simples e dupla (SMV e DMV, respetivamente), o que indica que o IAV conduz não só ao agrupamento vesicular mas também ao rearranjo das suas membranas (Vale-Costa et al. 2016).

Este trabalho permitiu fundamentar um modelo alternativo para a montagem genómica do IAV, em que o agrupamento vesicular pode funcionar como uma plataforma induzida pelo virus para a criação de *hotspots* de vRNPs. A alta co-localização entre o conjunto de todas as vRNPs permitiria a ocorrência das interações RNA-RNA necessárias à junção do genoma completo composto pelos oito vRNPs. O agrupamento vesicular surge assim como um passo essencial no ciclo replicativo do IAV. Pelo que, a definição da cronologia de eventos que levam à sua maturação e as alterações na composição vesicular tornam-se fundamentais para compreender os mecanismos de montagem genómica do IAV.

Neste trabalho experimental foi aplicada uma multi-metodologia de crio-microscopia eletrónica (EM). A razão da escolha dos métodos de crio-EM baseia-se na capacidade que estas técnicas têm para preservar os detalhes ultra-estruturais sem introduzirem os artefactos morfológicos de volume, forma e desnaturação de epitopos associados aos métodos cuja abordagem é puramente química (Studer et al. 1989). No entanto, para a sua aplicação, estes métodos tiveram que sofrer otimizações. Os mesmos permitiram elucidar o modo como a agregação vesicular se forma em células A549 que expressam constitutivamente GFP-Rab11 durante a infeção e qual a função das vesículas agregadas no ciclo replicativo do IAV.

A metodologia de crio-EM usada incorporou duas técnicas conhecidas na área: a técnica de congelamento de alta pressão e de fixação química por substituição a baixas temperaturas e a técnica de Tokuyasu. A primeira utiliza a baixa temperatura do azoto (-196ºC) e alta pressão (aproximadamente 2000 bar) para crio-imobilizar as amostras. A técnica permitiu a preservação celular para análise morfológica e a quantificação vesicular (sem introdução de artefactos de fixação química). A segunda técnica, Tokuyasu, também tira partido da baixa temperatura do azoto para crio-imobilizar as amostras e permite manter as estruturas hidratadas para uma imunomarcação ótima. Esta técnica foi usada para discernir a origem das estruturas vesiculares em estudo.

As metodologias usadas neste trabalho foram alvo de diversas otimizações, com o intuito de preservar as características ultra-estruturais o mais próximo possível do seu estado nativo (McDonald 2007). Na otimização da técnica de congelamento de alta pressão dois parâmetros foram avaliados: a vitrificação e a preservação morfológica das células GFP-Rab11. A vitrificação refere-se ao processo de transformação de um liquido em sólido sem cristalização. A cristalização induz artefactos nas células, reconhecíveis sob a forma de redes interligadas de espaços vazios onde outrora expandiram os cristais de gelo. Ambos os parâmetros de vitrificação e preservação morfológica são afetados pelo tipo de suporte de amostra utilizado para congelar, bem como pelo tipo de enchimento escolhido para preencher o espaço livre entre a amostra e o suporte. Os tipos de suporte para congelamento de amostras testados foram os discos planos e os suportes côncavos. O primeiro tipo – discos planos - permite o congelamento de células em camada única e foi testado em combinação com três tipos de enchimentos (hexadeceno, dextano a 20% (m/v) e albumina sérica bovina a 20% (m/v)). O segundo tipo – suportes côncavos – permite o congelamento em *pellet* e foram testados em combinação com hexadeceno. Estabeleceu-se que o melhor protocolo para processamento de células GFP-Rab11 por congelamento de alta pressão tendo em conta o objeto de estudo (a ultra-estrutura vesicular) foi alcançada ao usar a combinação de discos planos com hexadeceno.

Para a otimização da técnica de Tokuyasu, quatro marcadores: Golgi Marker (GM) 130, calnexina, nucleoproteína (NP) e GFP-Rab11 foram estudados em células infetadas com IAV para a capacidade de manter sua imunorreatividade em diferentes condições de fixação. Três fixadores foram usados durante o teste: formaldeído a 2% (v/v) com glutaraldeído a 0,2%, 0,1% e 0,05% (v/v). Como controlo foi adicionado o fixador de referência em imunocitoquímica: formaldeído a 4% (v/v). O formaldeído permite a manutenção da imunorreatividade celular, no entanto o glutaraldeído conduz a uma melhor preservação morfológica da ultra-estrutura. O fixador que permitiu a preservação da imunorreatividade de todos os marcadores foi o formaldeído a 4% (v/v) e, como tal, o fixador usado no estudo.

A combinação entre as técnicas de crio-EM, congelação por alta pressão e Tokuyasu, permitiu quantificar o número de vesículas de membrana simples e dupla (SMV e DMV, respetivamente) durante a infeção por IAV. Foi possível determinar que o número de SMVs - utilizadas como veículos para o transporte de vRNPs - aumenta durante a infeção por IAV e que as membranas destas vesiculas de membrana simples são reorganizadas para produzir as DMVs. Desta forma, é possível afirmar que as SMV juntamente com as DMVs parecem constituir os agregados vesiculares formados durante a infeção e que permitem a convergência espacial dos vRNPs.

Para além das técnicas de crio-EM descritas, também a técnica de correlação entre microscopia de luz e eletrónica (CLEM) foi desenvolvida e otimizada para pesquisa da função dos agregados vesiculares. A técnica de CLEM aplicada combinou as técnicas de hibridização *in situ* fluorescente (FISH), microscopia estocástica de reconstrução ótica (STORM) e EM e contribuiu para uma caracterização

adicional do papel das SMVs e das DMVs dentro dos agregados. A técnica FISH em conjunto com a técnica de STORM permitiu a identificação específica de segmentos do genoma do IAV em agregados de Rab11, enquanto a EM forneceu o contexto ultra-estrutural da célula. No entanto, a precisão da correlação alcançada foi baixa, não tendo permitido a identificação do conteúdo genómico transportado por cada vesícula dentro dos agregados. Neste sentido, podemos afirmar que, apesar de poder ser combinada com outras técnicas, a técnica de CLEM integrando FISH, STORM e EM é uma técnica ainda em desenvolvimento e que requer melhorias adicionais.

Em resumo, o trabalho aqui descrito conduziu à conclusão de que as vesículas de membrana simples e dupla, portadoras de vRNPs, são originárias do compartimento de reciclagem de endossomas. Ambos os tipos de vesículas foram encontrados nos agregados e identificadas com os mesmos marcadores imunes. A sua relevância funcional para a montagem dos vRNPs continua por inferir, sendo necessária a contínua otimização da combinação das técnicas de microscopia de luz e de microscopia eletrónica para determinar um método de CLEM funcional.

Palavras-chave: influenza A virus; agregação vesicular; Rab11; microscopia eletrónica; CLEM.

Abstract

Influenza viruses, from the *Orthomyxoviridae* family, are divided in four types A, B, C and D (Hause et al. 2013; Hause et al. 2014). Influenza A (IAV) as the capacity to generate zoonotic infections and is widespread in many mammalian and avian species. (Acheson 2011; Taubenberger & Kash 2010). In humans, IAV is the pathogen responsible for flu, a respiratory acute disease associated with high morbidity and mortality (Lofgren et al. 2007).

IAV as a segmented genome divided in eight different viral ribonucleoprotein complexes (vRNP). Each vRNP complex is composed by one of the eight viral ribonucleic acid segments. The vRNPs function as independent units and a complete set of eight different vRNPs is required for assembly of an infectious IAV particle (Fields et al. 2007).

It is known that vRNPs are transported by piggybacking in vesicles destined to the cell periphery via interaction between the viral polymerase basic protein 2 and the host GTPase Ras-related in brain 11 (Rab11) (Amorim et al. 2011; Eisfeld et al. 2011; Momose et al. 2011). Also, it was stated that during infection there is an aggregation of vesicles creating clusters. The clusters were composed by vesicles with single and double membranes (SMV and DMV), indicating that IAV leads not only to clustering but also to the rearrangement of vesicular membranes (Vale-Costa et al. 2016).

This work substantiated an alternative model for IAV genomic assembly in which vesicular clustering can function as a viral induced platform promoting the creation of vRNPs hotspots. The high co-localization among the pool of all vRNPs would allow the establishment (or completion) of the RNA-RNA interactions necessary for assembly of the eight RNA segments before budding. Vesicular clustering thus emerges as an essential step in IAV lifecycle.

In this work, a multi electron microscopy (EM) cryo-methodology was not just applied but also optimized and developed to elucidate how vesicular clustering is formed in A549 cells constitutively expressing GFP-Rab11 during infection and what the vesicles functional role in the lifecycle of IAV.

The EM cryo-methodology incorporated the High Pressure Freezing – Freeze Substitution (HPF-FS) and Tokuyasu techniques. The first permitted the morphological analysis of cells and vesicular quantification (without introducing chemical fixation artifacts) and the second enabled the immunolabeling of structures to discern their origin. Also, to further investigate the functional role of clusters a correlative light electron microscopy (CLEM) method that combines Fluorescent *in situ* Hybridization (FISH), Stochastic Optical Reconstruction microscopy (STORM) and EM was developed.

The optimization of HPF-FS technique established that the best vitrification and morphological preservation of GFP-Rab11 cells was achieved when using flat disks, as specimen carriers for the freezing process, filled with 1-hexadecene, as a cryoprotectant. For Tokuyasu, 4% (v/v) formaldehyde was the fixative to enable the best preservation of immunoreactivity.

Together, both techniques, lead to conjecture that the number of SMVs - used as vehicles for vRNP trafficking - increase during IAV infection and are modified to rearrange membranes and produce

DMVs. Both Rab11 SMVs and DMVs seem to constitute the clusters formed during infection that enable the spatial convergence of vRNPs.

The CLEM technique incorporating FISH, STORM and EM contributed to a further characterization of SMVs and DMVs role within the clusters. The FISH technique allowed the identification of IAV genome segments on Rab11 clusters imaged by STORM, whereas EM provided the ultrastructural context of the cell. A low accuracy of the achieved correlation did not allow the identification of the segment content of each vesicle within the clusters. This combinatorial but powerful method thus requires further improvement.

In summary, the work herein described led to the conclusion that vesicles of single and double membrane, carrying vRNPs, originate from the endosomal recycling compartment. Both types of vesicles were found in clusters. Their functional relevance for vRNP assembly remains to be determined, as the CLEM method developed for its study needs further optimization.

Keywords: influenza A virus; vesicular clustering; Rab11; electron microscopy; CLEM.

Table of Contents

Figures and Tables Index

Abbreviation List

APES	(3-Aminopropyl)triethoxysilane
BSA	Bovine serum albumin
CLEM	Correlative light electron microscopy
cRNA	Complementary RNA
DMEM	Dulbecco's modified eagle medium
DMV	Double membrane vesicle
EM	Electron microscopy
ER	Endoplasmic reticulum
ERC	Endosomal recycling compartment
FA	Formaldehyde
FISH	Fluorescent *in situ* hybridization
FS	Freeze substitution
GA	Glutaraldehyde
GM	Golgi marker
HA	Hemagglutinin
HPF	High-pressure freezing
IAV	Influenza A virus
LM	Light microscopy
M1	Matrix protein 1
M2	Matrix protein 2
MOI	Multiplicity of infection
mRNA	Messenger ribonucleic acid
MTOC	Microtubule-organizing center
NA	Neuraminidase
NP	Nucleoprotein
NS	Non-structural protein
OCT	Optimal cutting temperature compound
PA	Polymerase acidic protein
PB	Phosphate buffer
PB1	Polymerase basic protein 1
PB2	Polymerase basic protein 2
PBS	Phosphate-buffered saline
PI	Post-infection
Rab11	Ras-related in brain 11
RER	Rough endoplasmic reticulum
ROI	Region of interest
RT	Room temperature
SMV	Single membrane vesicle
STORM	Stochastic optical reconstruction microscopy
TEM	Transmission electron microscopy
vRNA	Viral ribonucleic acid
vRNP	Viral ribonucleoprotein complexes
WT	Wild-type

1. Importance of the Study

> "Disease cannot be understood unless it is realized that the ultimate abnormality must lie in the cell" – Rudolf Virchow

Influenza viruses, from the *Orthomyxoviridae* family, are obligatory intracellular parasites that rely on the host cell chemical energy, protein synthetizing machinery and controlled environment to replicate. They are divided in four types A, B, C and D (Hause et al. 2013; Hause et al. 2014). From these, influenza A (IAV) is a major threat to public health as it evolves exceedingly fast and is a zoonotic virus. The natural reservoirs of IAV are the wild aquatic waterfowl and shorebirds; however, due to stable host switches, the virus is widespread in many mammalian and avian species. (Acheson 2011; Taubenberger & Kash 2010).

There is a substantial diversity of circulating IAV virus subtypes classified by the nature of its surface glycoproteins: neuraminidase (NA) and hemagglutinin (HA). Eighteen HA (H1-H18) and eleven NA (NA1-NA11) types were identified and can be combined to generate the different IAV subtypes denominated HxNx depending on the surface glycoprotein content (Tong et al. 2013).

The subtypes are created by antigenic re-assortment which is made by a mechanism of antigenic shift. The antigenic shift is created when virus from different origins co-infect a host-cell and exchange genetic material. This mechanism have the capacity to created viral subtypes with different antigenic properties from the parental strains which can overcome the immune system and even break the inter-species barrier as reviewed in (Bouvier & Palese 2008).

In humans, IAV is the pathogen responsible for flu, a severe respiratory acute disease associated with high morbidity and mortality (Lofgren et al. 2007). Data from the World Health Organization, estimates that there are approximately 1 billion cases of flu every year, 3 to 5 million severe related illness hospitalizations and 300,000 to 500,000 associated deaths. In addition to yearly epidemics, IAV pandemics can also occur sporadically with associated devastating mortality. The most notable example is the "Spanish flu" originated from avian strains, between 1918 and 1920 caused around 40 million deaths. There are other cases worth mentioning, such as the "Asian flu" in 1957, also from avian origin but establishing in human via complex mixes (reassortment) with human viruses, and, more recently, the "Swine flu" in 2009, from swine origin (Saunders-Hastings & Krewski 2016).

IAV pandemics have up to now, been caused by infections with viruses unknown to the human immune system. In most cases the virus has crossed the host species barrier from avian and swine and established in humans. The ability of IAV to overcome the species barrier resides in the nature of its RNA segmented genome, divided in eight different particles called viral ribonucleoprotein complexes (vRNP). Each vRNP complex is composed by one of the eight viral ribonucleic acid (vRNA) segments individually wrapped with multiple monomers of the RNA-binding nucleoprotein (NP) and a heterotrimeric viral RNA polymerase composed by polymerase acidic protein (PA), polymerase basic protein 1 (PB1) and 2 (PB2) bound at the 3´ and 5´termini hairpin of the vRNA (Lee et al. 2017; Moeller et al. 2012; Arranz et al. 2012).

The vRNPs function as independent units for transcription and replication; however, for viral assembly, a complete set of eight different vRNPs is required increasing the complexity of genome

packaging. Identifying the mechanisms sustaining IAV genome is of utmost importance for human health. It has been widely reported that each segment has specific nucleotides located at the 3´ and 5´ termini responsible for RNA-RNA interactions that sustain the cohesion of the eight-segment core as reviewed in (Hutchinson et al. 2010). Much has been done to identify regions that are necessary for inclusion of the segments in virions (packaging signals) and for their binding to each other (bundling signals) (Giese et al. 2016). Recently it was suggested that the host recycling pathway facilitated IAV genome assembly.

After export from the nucleus, IAV replicated genome is trafficked in a two-step mechanism: 1) vRNPs accumulate nearby the microtubule-organizing center (MTOC) in the endosomal recycling compartment (ERC) and 2) piggyback onto vesicles destined to the cell periphery via interactions between viral PB2 and vesicular GTPase Ras-related in brain 11 (Rab11) (Amorim et al. 2011; Eisfeld et al. 2011; Momose et al. 2011). In homeostasis, Rab11 acts as a molecular switch regulating the steps involved in the processes of vesicle formation from the ERC, movement and fusion towards the plasma membrane being spread in the cytoplasm (Grant & Donaldson 2009). In infected cells, the Rab11 distribution pattern is altered and appears as a puncta indicating that IAV infection altered Rab11-vesicular pathway (figure 1) (Vale-Costa et al. 2016). During this transformation the co-localization of the eight different segments increased in a Rab11 dependent manner, and it was proposed that genome sub-bundling occurred *en route* from the nucleus to the actual budding site (Lakdawala et al. 2014; Chou et al. 2013).

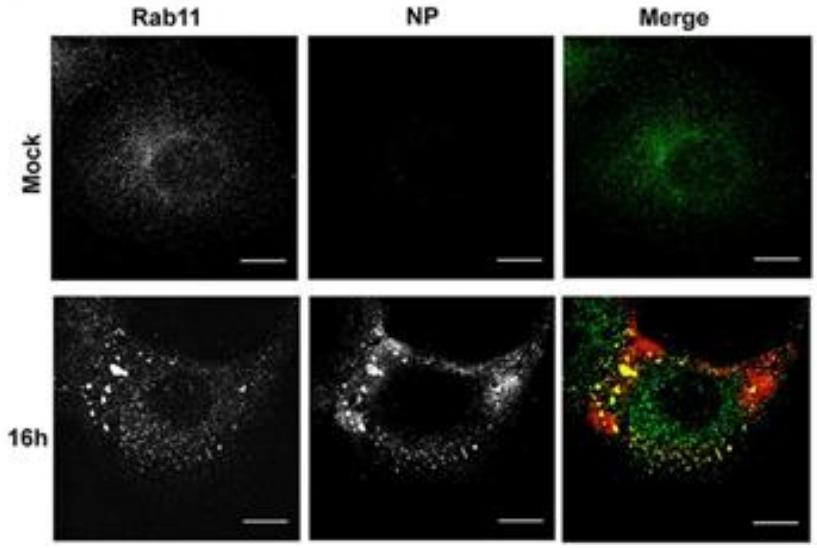

Figure 1. IAV infection alters Rab11 distribution

Immunofluorescence of A549 cells labeled for viral NP and Rab11. Mock cells represent the non-infected control and 16h cells represent the cells infected for 16 hours with influenza A/Puerto Rico/8/34 (PR8) at the multiplicity of infection (MOI) of 3. In mock cells, Rab11 is distributed homogeneously in the cytoplasm of the cell, having an accumulation at the perinuclear region where the MTOC is located. In infected cells, the Rab11 shows aggregation indicating that the infection with IAV leads to an alteration of Rab11 distribution pattern. Bar = 10 µm. Image adapted from our publications Vale-Costa et al. 2016.

Subsequently, I used correlative light electron microscopy (CLEM) methods to demonstrate the ultrastructural features underneath the Rab11 fluorescent signal (Vale-Costa et al. 2016). In this work it was observed that during infection there is an aggregation of vesicles, without fusion, creating clusters. The clusters were composed by vesicles of heterogeneous sizes with single and double membranes (SMV and DMV), indicating that IAV leads not only to clustering but also to the rearrangement of vesicular membranes (figure 2) (Vale-Costa et al. 2016).

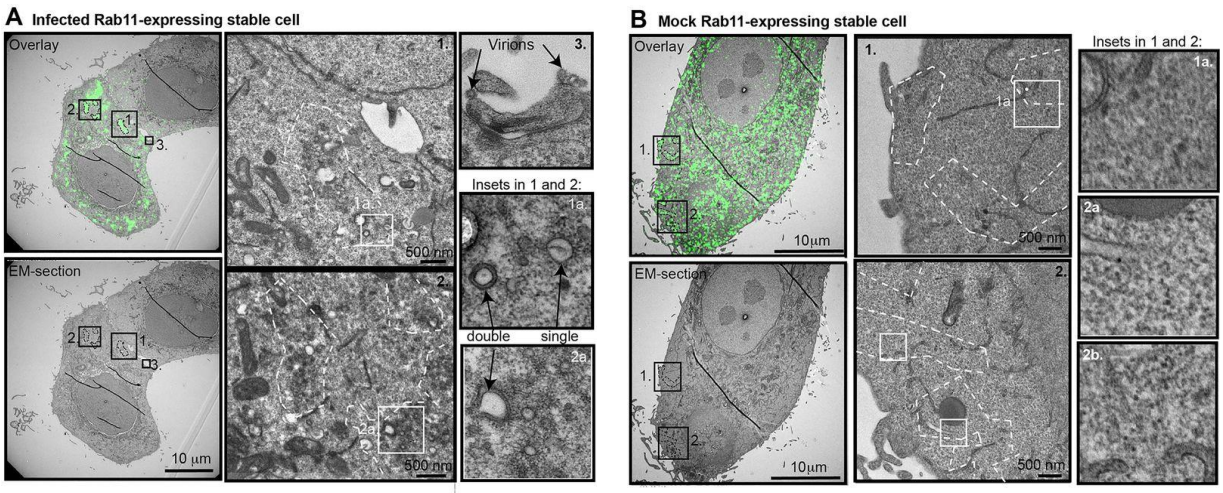

Figure 2. Ultrastructural features of Rab11 vesicular clustering revealed by CLEM technique

Correlative light electron microscopy (CLEM) of A549 cells expressing GFP-Rab11 and processed for Electron Microscopy (EM). **A.** Cells were infected for 16 hours with PR8 at a MOI of 3. ERC clustered vesicles are scattered in the cytosol. The clusters are composed by a heterogeneous population of vesicles with single and double membranes. **B.** Mock cells represent the non-infected control. No clusters of Rab11-vesicles were detected in the absence of IAV infection. Bar = 10 µm. Image adapted from our publications Vale-Costa et al. 2016.

This work substantiated an alternative model for IAV genomic assembly in which vesicular clustering can function as a viral induced platform promoting the creation of vRNPs hotspots. The high co-localization among the pool of all vRNPs would allow the establishment (or completion) of the RNA-RNA interactions necessary for assembly of the eight RNA segments before budding. Vesicular clustering thus emerges as an essential step in IAV life cycle. The definition of the chronology of events leading to maturation of vesicular clusters, in particular formation of clusters and alterations in vesicular composition become central to understand the mechanisms of IAV genome assembly.

In the present work, electron microscopy (EM) cryo-methods were applied to further investigate our IAV genome trafficking and assembly model. These methods are crucial in order to define the smallest ultrastructural details hindered by the chemical approaches (Studer et al. 1989). Despite the advantages of using the EM cryo-methods, without the appropriate optimization and development they cannot be used to their full potential (Roingeard 2008; Romero-Brey & Bartenschlager 2015).

In summary, within this work the EM cryo-methodologies were not just applied but also optimized and developed to elucidate how vesicular clustering is formed during infection and what is its functional role in the lifecycle of IAV.

2. Research Approach

2.1 Study Location

This study was developed in the laboratory of Cell Biology of Viral Infection laboratory and in the Electron Microscopy Facility, at the Instituto Gulbenkian de Ciência located at Rua da Quinta Grande 6, 2780-156 Oeiras, Portugal.

2.2 Research Question and Hypothesis

The vesicular clustering is formed during IAV infection and plays a role in viral lifecycle, promoting the establishment of RNA-RNA interactions among the different segments.

2.3 Objectives

2.3.1 General Objectives

a) Characterise the biogenesis of the vesicles that cluster during IAV infection;

b) Determine the functional relevance of vesicular clustering for IAV genome assembly.

2.3.2 Specific Objectives

a) Optimize an electron microscopy (EM) cryo-method for the preparation of A549 cells constitutively expressing GFP-Rab11 cells evaluating the vitrification rate and morphological preservation;

b) Quantify the number of vesicles of single and double membrane (SMV and DMV) over an IAV infection time-course using the EM cryo-method assessed in specific objective a);

c) Describe the morphological profile of the cellular structures involved in cluster formation during IAV infection using tomography and 3D modeling;

d) Optimize a fixation method that enables immuno-gold labeling and ultrastructural identification to determine the origin of the vesicular content of clusters;

e) Develop a CLEM method to image individual IAV vRNPs in A549 cells constitutively expressing GFP-Rab11 infected cells using super resolution light microscopy and EM.

3. Literature Review

"A thorough, sophisticated literature review is the foundation and inspiration for substantial, useful research" – D. Boote and P. Beile

3.1 Influenza A Virus

3.1.1 Structure

IAV is a pleomorphic virus that can assume spherical or filamentous forms. The spherical particles have approximately 100 nm in diameter and the filamentous ones have 300 nm in length (Mosley & Wyckoff 1946). The virion is composed by a host-derived envelope with an external layer of spike-like projections. This layer surrounds the segmented negative-strand RNA genome (figure 3), characteristic of the *Orthomyxoviridae* family, where IAV belongs (Fields et al. 2007).

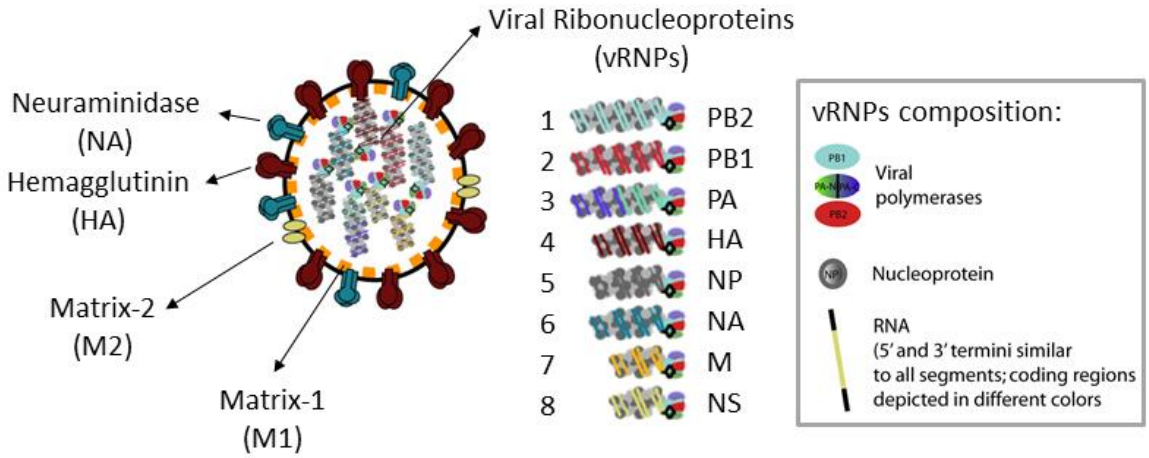

Figure 3. IAV virion structure

IAV is composed of a lipid envelope that contains three structural proteins: hemagglutinin (HA), neuraminidase (NA) and matrix protein 2 (M2). The viral core is coated with the matrix protein 1 (M1), and encloses the viral genome composed by eight vRNPs. Each vRNP encodes for different viral proteins and is composed by the hetero-trimeric viral polymerase (PB1, PB2 and PA) and the negative-sense vRNA genome wrapped by NP. Image produced by Maria João Amorim.

3.1.1.1 Viral Envelope

The virion has a host cell derived lipid envelope that contains three transmembrane proteins HA, NA and matrix protein 2 (M2). M2 is a minor component of the virion envelope, whereas HA appears in larger number followed by NA (Compans et al. 1970; Hutchinson et al. 2014). There are 18 genetically different subtypes of HA and 11 of NA (Tong et al. 2013). IAV is classified by the expression of different combinations of HA and NA subtypes at the virion surface (Fields et al. 2007).

HA is synthetized as a precursor protein (HA0) at the rough endoplasmic reticulum (RER), matured at the Golgi complex and transported to the plasma membrane, where is cleaved by cellular proteases to form HA1 and HA2. HA1 and HA2 remain linked through a disulphide bond to form the HA monomer (Rodriguez-Boulan et al. 1984; Braakman et al. 1991; Lamb, Robert and Choppin 1983). HA is presented at the surface of the virion as a homotrimer. It is responsible for: 1) viral recognition and binding to the sialic acid cellular receptor and 2) membrane fusion between the viral envelope and the host cell membrane (Wiley & Skehel 1987).

NA is presented as a homotetramer at the virion surface (Varghese et al. 1983). It cleaves the sialic acid present in glycoproteins or glycolipids from the cell surface and also on oligosaccharides from mucoproteins. This enzymatic activity mediates the release of newly formed virions from the surface of the host cell and from the abundant mucins present in the respiratory tract (Matrosovich et al. 2004).

The third transmembrane protein, M2, also forms a homotetramer. It functions as an ion channel modulating the pH within the virions. It allows a flow of ions from the endosome across the virion envelop that results in the virion acidification. This process disrupts the connection between the matrix protein 1 (M1) and the vRNPs in the viral core and enables the release of the uncoated vRNPs into the cytoplasm (Holsinger et al. 1994; Pielak & Chou 2011).

3.1.1.2 Viral Core

IAV viral core is enclosed by an internal layer of the matrix protein, M1. M1 covers the inner part of the lipid layer and interacts with the vRNA and the NP holding the vRNP complex structure together. Also, it is involved in the nuclear export of IAV genomic segments together with the nonstructural protein (NS) 2 (Fields et al. 2007). The NS2, also called nuclear export protein, binds to cellular export proteins and nucleoporins recruiting the machinery necessary for nuclear exportation of the complex M1-vRNPs (O'Neill et al. 1998).

There are eight individual vRNPs complexes that together constitute the viral genome (McGeoch et al. 1976). Each composed by a negative-sense single stranded vRNA segment with regions bound to multiple copies of NP and regions NP-free (Lee et al. 2017). Each of the eight genome segments encode for a major viral proteins: PB2, PB1, PA, HA, NP, NA, M and NS (figure 3). However, from this major proteins, ten other viral proteins arise by splicing, ribosomal frameshifts or alternative initiation (Yamayoshi et al. 2014).

The vRNA segment 4, 5 and 6 encode for a single protein each: HA, NP and NA, respectively (Palese & Schulman 1976; Ritchey et al. 1976). The segment 1 encodes for PB2 and PB2-S1 (Yamayoshi et al. 2014), the segment 2 for PB1 and the accessory protein PB1-F2 and PB1-N40 and the segment 3 for PA, PA-N155, PA-N182 and PA-X (Akkina 1990; Chen et al. 2001; Wise et al. 2009; Jagger et al. 2012). Also, the two last segments 7 and 8, encode for the matrix proteins M1, M2 and M42 and for the non-structural proteins, NS1, NS2 and NS3, respectively (Wise et al. 2012; Selman et al. 2012). The vRNPs can be also divided by length in three categories: 90-110 nm (segments 1-3), 60-90 nm (segments 4-6) and 30-50 nm (segments 7-8) (Zheng & Tao 2013).

At the 5´ and 3´ termini of the each segment there is 13 and 12 conserved nucleotides, respectively, that form a hairpin structure to where is connected the heterotrimeric viral RNA-dependent RNA polymerase composed of PA, PB1 and PB2 (Moeller et al. 2012; Lee et al. 2017). There are noncoding regions at both 3´ and 5´ ends with a highly conserved region in the extreme end that functions as a promoter for the replication and transcription by the viral polymerase. These regions also possess a messenger RNA (mRNA) polyadenylation and packaging signals (Lamb, Robert and Choppin 1983; Fields et al. 2007).

3.1.2 Lifecycle

The lifecycle of IAV can be categorized in five major steps: 1) Entry; 2) Uncoating; 3) Replication; 4) Trafficking and 5) Assembly, budding and release (figure 4).

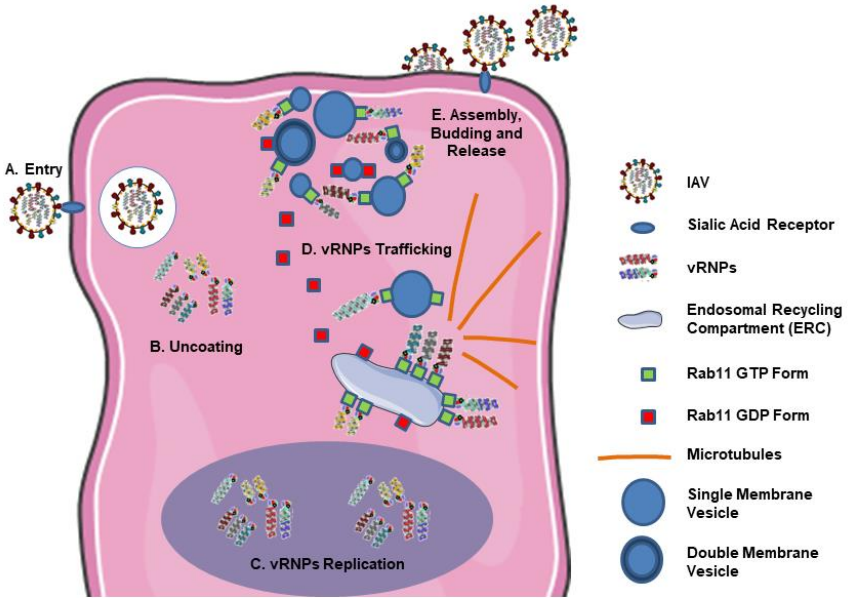

Figure 4. IAV lifecycle

A. IAV binds to host sialic acid receptors at the cell membrane and enters via endocytosis. **B.** Once inside, the fusion between the endosomal membrane and the viral envelope is triggered with consequent release of the vRNPs onto the cytosol. **C.** The vRNPs are transported to the nucleus, where the replication of vRNA happens. **D.** After replication, the vRNPs are accumulated at the ERC and transported via Rab11-vesicles towards the cell periphery. **E.** In the periphery occurs the assembly of the complete genomic set and the incorporation onto the viral envelope, before budding and release of the progeny particles.

3.1.2.1 Entry

The first step of the IAV lifecycle is the entry of the virion in the host cell (figure 4A). The step starts with the recognition and attachment of the virus to the target cell. The viral protein HA (or HA0 for the non-cleaved form) requires activation through cleavage into HA1 and HA2 by host proteases. HA1 recognizes the sialic acid cell receptor located on glycoconjugates at the cellular membrane (Rossmann & Rao 2012).

The sialic acid is connected to a galactose residue by a glycosidic linkage that can assume an α2,3 or α2,6 configuration. The different subtypes of HA have a fine specificity towards the type of configuration. For example, human influenza strains with human adapted HA subtypes, binds to α2,6 linkage configuration rather than α2,3 and avian influenza does the opposite (Connor et al. 1994). After attachment, the influenza virion penetrates the cell via receptor-mediated endocytosis (Matlin et al. 1981; Rust et al. 2004).

3.1.2.2 Uncoating

Uncoating and subsequent release of the vRNPs into the cytosol is mediated by the endosomal acidic environment (pH 5-6). During the process two key steps occur: the fusion between the endosomal membrane and the viral envelope and the release of the vRNPs from the M1 matrix. In the first step, HA conformational rearrangements are triggered. The hydrophobic fusion peptide of the HA2 domain is exposed and is inserted into the endosomal membrane to create a fusion pore (Skehel & Wiley 2000). In the second step, the hydrogen ions present in the endosome are pumped via the viral M2 towards the core of the virion (Kemler et al. 1994). This disrupts the interactions between M1 and vRNPs. The two steps enable the direct release of vRNPs onto the host cytosol (figure 4B).

3.1.2.3 Replication

The vRNPs released into the cytosol are transported to the cellular nucleus (figure 4C) by a process that involves the importin α pathway recognition of the vRNPs structural component nucleoprotein (O'Neill et al. 1995; Neumann et al. 1997). There, the process of transcription and replication occurs via a mechanism that is being unraveled by many scientists for many years and is reviewed in (te Velthuis & Fodor 2016). The negative-sense vRNA is used as a template for two positive-sense products: mRNA, for viral protein translation, and complementary RNA (cRNA), the latter serving as a template for synthesis of multiple copies of negative-sense vRNA by the viral RNA-dependent RNA polymerase (te Velthuis & Fodor 2016).

The viral mRNA contains a 5´ cap sequence and a poly-A tail at the 3´ termini (Lamb, Robert and Choppin 1983). The viral RNA-dependent RNA polymerase hijacks the host pre-mRNA cap regions through a process of "cap snatching". The subunit PB2 recognizes cap structures on host pre-mRNAs (Ulmanen et al. 1981; Peng et al. 1996), PA cleaves these structures (Dias et al. 2009) and PB1 has polymerase activity that elongates transcripts (Braam et al. 1983). The cap regions function as primers for viral mRNA synthesis and are also essential for the efficient binding of ribosomes to the mRNA. Through the cap snatching process, IAV promotes the production of viral components and inhibits host mRNA translation and consecutive protein synthesis. This process disrupts the cellular homeostasis and eventually leads to cell death. The poly-A tail of viral mRNAs is a host independent process that results from stuttering of a poly-U stretch in vRNA templates (Robertson et al. 1981).

The viral mRNA is transported to the cytoplasm where translation of both viral envelope and core proteins happens. The viral envelope proteins NA, HA and M2 are synthetized in the cytosol and transported to the endoplasmic reticulum (ER) where they are glycosylated and folded into trimers and tetramers (Braakman et al. 1991; Fields et al. 2007). After folding they are transported through the Golgi apparatus and the trans-Golgi network to the plasma membrane as reviewed in Bouvier & Palese 2008. The viral core proteins, PA, PB1, PB2 and NP are translated and sent to the nucleus to first promote the vRNA replication and second to join the newly replicated vRNA. M1 and NS2 are also translated and imported to the nucleus to assist vRNP export to the cytoplasm (O'Neill et al. 1998; Bui et al. 2000). Part of M1 is transported to the plasma membrane where it interacts with NA and HA C-terminal domains.

3.1.2.4 Trafficking

After nuclear export, vRNPs need to be transported towards the plasma membrane for assembly, budding and release (Fields et al. 2007). The trafficking of the genome is made in a two-step mechanism: first the vRNPs agglomerate at the perinuclear region and second piggyback onto Rab11 vesicles of the endosomal recycling compartment (ERC) to be transported on microtubules towards the cell surface (figure 4D) (Amorim et al. 2011; Eisfeld et al. 2011; Momose et al. 2011).

Rab11 is a GTPase involved in the recycling of endocytosed proteins. It regulates vesicle formation from the ERC, movement and fusion as reviewed in (Grant & Donaldson 2009). It was also described as being implicated in the exocytosis of the ERC vesicles (Takahashi et al. 2012). It acts as a molecular switch with GDP/GTP cycles. Rab11-GDP is the inactive form. It connects to dissociation inhibitors (Rab-GDIs) that delivers Rab11 to target membranes. At the membranes, guanine exchange factors activates Rab11 by changing GDP to GTP. The activated form, Rab11-GTP, can be connected to effectors that mediate the movement and fusion of vesicles with target membranes. The inactivation is made by guanine-activating proteins that hydrolyse GTP. This process leads to a decrease in the

affinity between Rab11 and the effectors. Rab11-GDP is recycled back to the cytoplasm by Rab-GDIs (Pasqualato et al. 2004; Vale-Costa & Amorim 2016).

In homeostasis Rab11 is spread throughout the cytoplasm; Whereas in IAV infected cells, Rab11 forms large cytoplasmic aggregates (Vale-Costa et al. 2016). The most recent model proposes that Rab11 aggregates form a viral induced platform for the spatial converging of vRNPs before assembly and budding (Chou et al. 2013; Lakdawala et al. 2014). This platform is composed by clusters of heterogeneous vesicles with single and double membranes (Vale-Costa et al. 2016).

3.1.2.5 Assembly, Budding and Release

Virion assembly comprises the incorporation of viral genome and proteins and occurs at the plasma membrane. Interestingly, in the case of IAV it is possible that viral assembly comprises two steps: the assembly of the viral genome (via a bundling process), composed of eight distinct segments and its packaging (inclusion) into budding virions at the plasma membrane. It is known that to create an infectious particle each virion needs to incorporate a complete genomic set of eight different vRNPs (Hutchinson et al. 2010).

A lot of research was conducted to solve a long standing debate of whether packaging was a selective or a random process, but overwhelming evidence indicates that the packaging process is selective and occurs through RNA-RNA interactions between the different vRNPs that contain specific packaging signals located at the 5´and 3´ termini (Giese et al. 2016)

Regarding assembly of IAV genome, recently exciting data has been published. Using multicolor fluorescence *in situ* hybridization two groups have shown that several segments co-localize in the cytoplasm and proposed that genome assembly could occur *en route* to the plasma membrane, favored by kissing and/or fusion events between vRNP-carrying vesicles (Chou et al. 2013; Lakdawala et al. 2014). These studies used confocal microscopy that lacks the resolving power to distinguish between association of vRNPs or simple spatial convergence in the cell cytoplasm.

We have used electron microscopy (EM) to address this question and found that vRNPs converged in space in regions of clustered vesicles that carry vRNPs facing the cytosol (Vale-Costa et al. 2016). Even with EM resolution, we were unable to find proof of association between the distinct vRNPs. This observation did however lead to the proposal of an alternative model for IAV genome assembly: vesicular clustering leads to formation of vRNP hotspots containing the eight segments and might facilitate genome assembly downstream. Doubt remains of where genome assembly occurs, if before reaching the membrane or at the budding site. In budding virions the eight vRNPs were visualized by EM almost pulling the membrane to be accommodated inside a virion (Fournier et al. 2012; Noda et al. 2012).

On the plasma membrane, the vRNPs interact with the M1 viral protein attached to the internal domain of NA and HA (figure 4E). After budding, lAV is released from the cell surface via the action of M2 and NA. M2 is involved in the scission the budded virion and NA cleaves the host sialic acid that attaches viral HA to the cell surface (Fields et al. 2007; Rossman et al. 2010).

3.2 Electron Microscopy Cryo-Methods to Study IAV at the Nanoscale

The visualization of the ultrastructural alterations induced by infection requires the application of methods whose resolution achieves the nanoscale, such as EM. Despite the advantages of the

resolution attained by EM, without appropriate methods to prepare samples, it cannot be used to its full potential to the research of viruses and the mechanisms of viral replication (Roingeard 2009; Romero-Brey & Bartenschlager 2015).

The major goal of EM methods is to preserve the ultrastructural features as close as possible to their living or native state (McDonald 2007). For that reason, fixation is one of the most critical steps during sample preparation (Bancroft & Gamble 2002). There are two types of fixation methods: chemical and physical.

The chemical fixation is typically executed with aldehydes that react with basic amino-acid residues on proteins. Such reaction creates methylene bridges between proteins, thus originating a network of crosslinks (Bancroft & Gamble 2002). The aldehydes usually employed are formaldehyde (FA) and glutaraldehyde (GA), composed by one or two aldehyde reactive groups, respectively. The higher cross-linking capacity of GA causes greater loss of protein structure and immunological activity than FA; however, GA preserves the morphology better (Bancroft & Gamble 2002).

Physical fixation, also called cryo-immobilization, uses cryogens instead of chemicals to stabilize cellular components. This process avoids the distortions induced by chemical fixation but it is limited by the water content of biological sample. Water is a poor heat conductor and limits the cooling rates within the sample leading to crystallization (Romero-Brey & Bartenschlager 2015).

Both fixation methods can be combined when handling infectious samples, such as IAV infected cells. The chemical inactivation of the virus is required prior to cryo-immobilization for the safe handling of the specimens. Two cryo-methods where the hybrid fixation can be employed are the High Pressure Freezing (HPF**)** - Freeze Substitution (FS) and the Tokuyasu techniques.

3.2.1 High Pressure Freezing – Freeze Substitution

The HPF is a freezing technique that cryo-immobilizes the sample by high pressure (around 2000 bar) and low temperature (-196ºC). This combination alters the physical properties of water by lowering its freezing point. The growth rate and nucleation of ice crystals is reduced and enables water vitrification before crystal formation (Moor 1987).

After cryo-immobilization by HPF, the most common way to process the cells is by FS (McDonald 2007). FS replaces the frozen water by an organic solvent, such as acetone, at a low temperature, avoiding the artifacts introduced by dehydration at room temperature (RT) (Morphew 2000). Also, a fixative can be added to the solvent, *e.g.* uranyl acetate. At -90ºC, the fixatives will penetrate the sample but will be inactive. This means that the fixative is homogenously distributed through the cell and simultaneously fixes all components when the sample is warmed to the fixative reactive temperature (McDonald 2007). After FS, the samples can be embedded in resin, sectioned by ultramicrotomy and analysed by transmission electron microscopy (TEM).

For a successful HPF-FS of cells, one of the most important steps is the loading of samples into the high pressure freezer machine (McDonald 2007). Several types of specimen carriers and fillers, differing in material and geometry, are available depending on the manufacturer (McDonald 2007; Morphew 2000). Two examples are hats and flat disks. The following described carriers belong to the High Pressure Freezer Compact 02 (Wohlwend Engineering Switzerland).

Hats can be made of aluminum with an excellent thermal conductivity of 200-250 W/(m.K) (Verkade & Muller-Reichert 2012). The aluminum hats are round cups with an external diameter of 3 mm and internal diameter of 2 mm (figure 5A). The inner cavity depth can range from 0.025 mm to 0.3 mm, and two hats can be combined in multiple arrangements to form a chamber ranging from 0.025 mm to 0.6 mm in depth. Hats can be used to freeze a high number of cells in a pellet (McDonald 2007).

Flat disks can be made of aclar (figure 5B), that has a thermal conductivity of 0.19-0.22 W/(m.K) (Verkade & Muller-Reichert 2012). For freezing, flat disks need to be combined with a 0.04 mm hat to form a chamber. Flat disks permit growing and freezing cells in a monolayer.

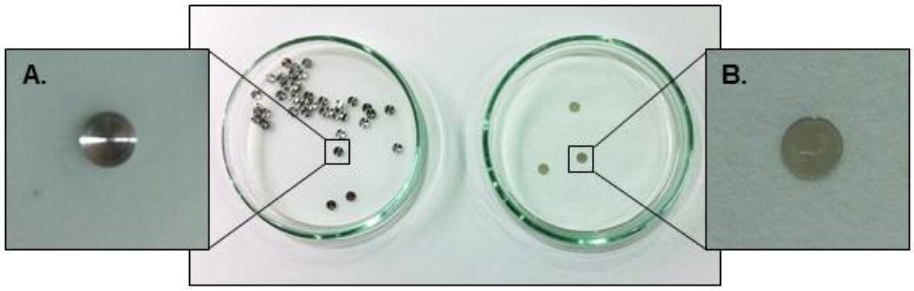

Figure 5. Specimen carrier and aclar flat disk example

There are several types of specimen carriers available whose design varies between HPF manufacturers. **A.** Hats made of aluminum with a depth of 0.1 mm. For freezing they need to be combined to form a chamber where the sample resides. **B.** Flat disks made of aclar. These disks can be used for the growth of monolayers and also need to be combined with a special hat of 0.04 mm for freezing.

Both types of sample carriers need a filler to occupy the space surrounding the cells and minimize the aqueous material to be frozen (Morphew 2000). The fillers should have good heat transfer properties and bind to water molecules to avoid their rearrangement into crystals (McDonald 2007).

The fillers can be intracellular or extracellular. Extracellular are preferred since they do not penetrate and interfere with the internal structure of cells (McDonald 2007). Some examples of extracellular fillers are: 1-hexadecene, dextran and bovine serum albumin (BSA).

3.2.2 Tokuyasu

Tokuaysu is an EM cryo-method that enables the preparation of frozen-hydrated specimen for cryosectioning and immunolabeling. Cells are primarily fixed in aldehydes, cryo-protected with 2.3 M sucrose and plunge frozen in liquid nitrogen (Griffiths 1993). Sucrose is an intracellular cryo-protector that avoids cellular crystallization and, together with the aldehyde fixation, gives enough consistency to the cells so they can be ultracryosectioned (Tokuyasu 1973).

This technique is the gold-standard for TEM immunogold labeling (Mobius 2009). The sections remain hydrated and the antigens accessibility is not hindered by the presence of a resin. Nevertheless, for high-resolution localization of antigens, the initial fixation must permit a balance between ultrastructure and immunoreactivity preservation. Aldehyde induced cross-linking must be weak enough to maintain epitope accessibility yet preserving ultrastructural morphology. This balance needs to be optimized according to the biological system in study and the sensitivity of the antigens to be detected. Optimization should be done by light microscopy (LM) to avoid lengthy and labor-intensive EM procedures (Morphew 2000).

3.2.3 Correlative Light Electron Microscopy

Correlative light electron microscopy (CLEM) methods emerged as a powerful tool in the field of cellular biology. They allow the imaging of the same structure using two microscopy modalities, LM and EM (Verkade & Muller-Reichert 2012). LM enables the identification of fluorescence/colorimetric tags widely used while EM allows correlating such tags with the ultrastructure within the cellular context (Verkade & Muller-Reichert 2012). These tags can be endogenously expressed by the cell or added externally, for example through immunocytochemistry or fluorescent *in situ* hybridization (FISH). With the development of new techniques, such as LM super-resolution, a number of different and new CLEM approaches has arisen.

3.2.3.1 STORM, FISH and EM to Study IAV genome

Stochastic optical reconstruction microscopy (STORM) is a type of super-resolution microscopy. It uses a sequential activation and then time-localization of fluorophores with photo-switchable capabilities. At each time-point only a subset of fluorophores is activated to a fluorescent state. Their position is recorded and its centroid position is precisely found. Then this set of fluorophores is inactivated and the cycle is repeated in several acquisitions of different fluorophore sets. Finally, fluorophore positions can be reconstructed to give rise to a high-precision LM image (Rust et al. 2006). STORM can be allied to techniques such as FISH in order to detect fluorescent dyes attached to nucleic acids.

FISH uses complementary genomic sequences attached to fluorescent probes to detect specific parts of the genome (Bancroft & Gamble 2002). For our purpose, it can be used to localize specific viral genome segments in IAV infected cells. For performing the technique, the cells need to be permeabilized so the probes can reach the intracellular targets. There are two types of permeabilization: chemical and physical. The chemical permeabilization cannot be used for EM, since it disrupts the ultrastructure. Instead, cells can be opened through physical permeabilization with sectioning (McDonald 2007).

The sectioning can be done before or after the EM processing. The pre-processing sectioning can be done using a cryostat or vibratome (Vogels et al. 2009). It facilitates the accessibility of the probes to the targets and enables further processing of sections with heavy metals for high-contrast ultrastructural preservation. Within this work, the pre-processing approach was used, with the FISH labeling being done in cryostat sections. The FISH labeling on cryostat sections is a common approach, however some points need to be adapted for the later STORM imaging, EM processing and correlation of techniques.

4. Material and Methods

"Setting a goal is not the main thing. It is deciding how you will go about achieving it and staying with that plan" – Tom Landry

4.1 Cell Culture

Human alveolar basal epithelial A549 cells expressing GFP-Rab11 Wild-Type (WT) were cultured with Dulbecco's Modified Eagle Medium (DMEM) (®Life Technologies) supplemented with 2 mM glutamine, 50 µg/ml streptomycin, 50 U/ml penicillin (®Biowest) and 10% (v/v) fetal bovine serum. Cells were maintained in T75 flasks at 37ºC in a humidified atmosphere with 5% CO_2. The cells were sub-cultured every 3-4 days. The procedure consisted in: 1) rinsing cells with phosphate-buffered saline (PBS), 2) trypsinizing with 1 µg/mL solution of trypsin in PBS for 5 minutes at 37ºC, 3) pelleting by centrifugation and 4) resuspending in DMEM accordingly to the desired confluence.

4.2 Infection

Cells were infected with IAV A/Puerto Rico/8/34 (PR8; human subtype H1N1) at a multiplicity of infection (MOI) of 5 in serum-free-DMEM for 30 minutes. Afterwards, infection was stopped by the addition of DMEM and cells were incubated at 37ºC in a humidified atmosphere containing 5% CO_2 (Amorim et al. 2011).

4.3 Morphology and Quantification

4.3.1 High Pressure Freezing

Two types of HPF sample preparation were tested: pellet and monolayer (figure 6 A and B, respectively).

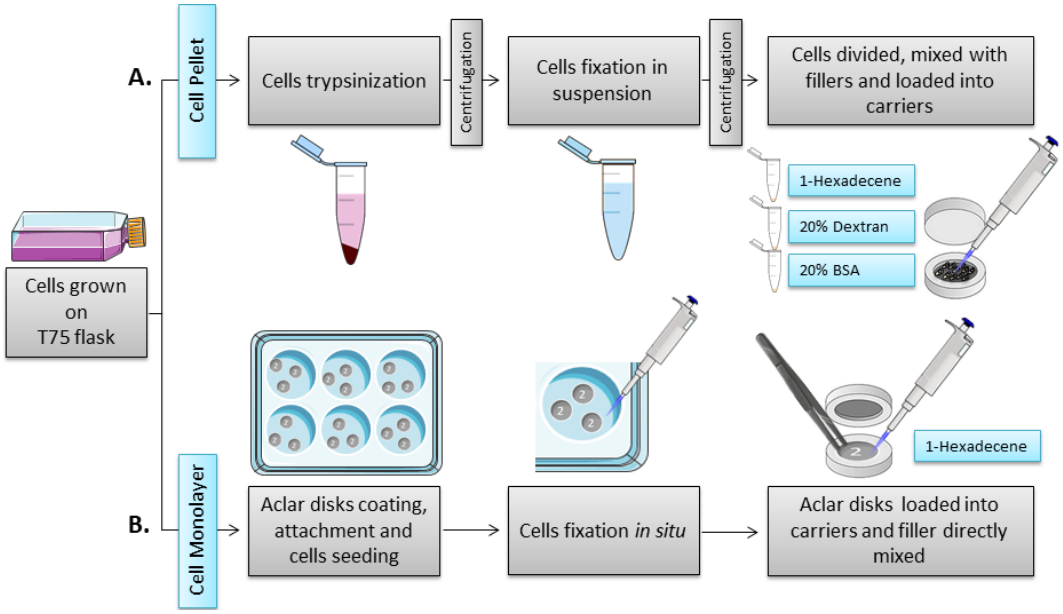

Figure 6. Scheme of HPF optimization

Two types of cell preparations were tested for HPF of cells: pellet or monolayer. **A.** For pellets, cells were trypsinized and fixed in suspension. In the last step, the pellet was divided to test three fillers: 1-Hexadecene, 20% (w/v) Dextran and 20% (w/v) BSA. The cells mixed with the fillers were pipetted to the carrier. **B.** For monolayers, cells were seeded in plates previously prepared with aclar disks coated with carbon and engraved with the number "2" for orientation. Cells were fixed in the plate. In the last step, the aclar disks were removed with forceps and loaded into the carrier with the engraved side with the number "2" facing up. The filler, 1-Hexadecene, was added directly to the carrier containing the aclar disk.

For the pellet method, cells were seeded in T75 flasks at a density of $5x10^4$ cells/ml, washed with PBS, trypsinized and pelleted by centrifugation (200 rcf, 5 minutes). For the monolayer preparation, cells were seeded at a density of $4x10^4$ cells/ml onto 3 mm aclar disks attached with dental wax to a 6 well-plate. Prior to seeding, the aclar disks were coated with a layer of carbon and then landmarked with the number "2" using a needle. This was done to track the side of the disk where the cells were seeded – when the number "2" was readable, the cells were on the top. Cell monolayers were fixed *in situ*, whereas pellets were fixed in suspension both using a mixture of 2% (v/v) formaldehyde (FA) (®EMS) and 0.2% (v/v) glutaraldehyde (GA) (®Polysciences) in 0.1M phosphate buffer (PB), for 2 hours at RT. Cells were washed with PB in between the steps. Pellets were additionally centrifuged and resuspended before loading in carriers. The pellet was loaded into 0.1 mm deep carriers and, due to the thickness of the pellet, three types of fillers were tested: 1-Hexadecene (®Merck), 20% (w/v) Dextran (®Alfa Aesar) and 20% (w/v) BSA (®Sigma Aldrich). The monolayers in the aclar disks were added to a 0.04 mm deep carrier which was filled with 1-hexadecene. Hexadecene was used in this case since it has a low viscosity and surface tension that reduces the air trapped in the carriers (Studer et al. 1989). All samples were frozen using a High Pressure Freezer Compact 02 (®Wohlwend Engineering Switzerland).

4.3.2 Freeze Substitution

For FS the Leica EM AFS2 was used together with a processor Leica EM FSP. The samples were freeze substituted at -90ºC with 0.1% (w/v) uranyl acetate and 0.01% (w/v) tannic acid (®EMS) in acetone for 6 hours. The temperature was raised to -45ºC at a slope of 5ºC/hour. Samples were stabilized at -45ºC for 1.5 hours before washing in acetone three times. Samples were infiltrated and embedded in Lowicryl HM20 (®Polysciences) at -45ºC. Polymerization of the resin was done using ultraviolet light at -25ºC for 48 hours.

4.3.3 Ultramicrotomy and Post-Staining

Sections were taken at 70 nm for 2D imaging. The sections from the flat disks blocks were picked at 1.2 µm starting from the cell bottom. For tomography 120 nm sections were cut. The sectioning was performed on a Leica UC7 and all the sections were picked on palladium-copper grids coated with 1% (w/v) formvar (®Agar Scientific) in chloroform (®VWR). The post-staining was made with 1% (w/v) uranyl acetate and Reynolds lead citrate, for 5 minutes each. For tomography, 15 nm protein A-gold (®UMC, Utrecht) was added to both sides of the sections before staining.

4.3.4 Data Acquisition

The images for technique optimization were acquired on a Hitachi H-7650 operating at 100 keV equipped with a XR41M mid mount AMT digital camera. For quantification and morphology analysis, photomontages and tomograms were acquired on a FEI Tecnai G^2 Spirit BioTWIN operating at 120 keV equipped with a Olympus-SIS Veleta CCD Camera.

4.3.5 Data Analysis

4.3.5.1 High Pressure Freezing – Freeze Substitution Technique Optimization

For the optimization of the HPF-FS technique two parameters were studied: vitrification rate and morphology preservation.

A. Vitrification Rate

Tested conditions: Two types of specimen carrier were tested: aluminum hats 0.1 mm deep and aclar flat disks. For the hats, three types of cryo-protectants were tested: 1-hexadecene, 20% (w/v) Dextran and 20% (w/v) BSA. For the flat disks and due to the reduced thickness of sample only 1-hexadecene was used for evaluation.

Sampling: For each condition, five blocks were produced. From each block, one section was taken and one cell was randomly imaged. For each cell, three pictures at the magnifications of 1k, 5k and 10k were acquired on a Hitachi H-7650 equipped with a XR41M mid mount AMT digital camera.

Criteria: Cells with absence of crystallization patterns are vitrified (Studer et al. 1989). Cells with good vitrification were classified with an arbitrary value of 1 and cells with ice damage were categorized as -1. To all images a randomized numerical code was given to allow a non-biased evaluation. The classification was performed by three different evaluators. Results were presented as % of vitrified blocks relative to a total number of blocks without ice damage. The number of blocks was directly translated from the number of vitrified cells, since each cell correspond to one single block.

B. Morphology Preservation

Tested conditions: Aclar flat disk frozen with 1-hexadecene and 0.1mm aluminum hats with 20% (w/v) dextran. The two types of specimen holders involve different cellular preparations that can influence the ultrastructure preservation; however, to reduce the number of conditions, only the cryo-protectant condition from the aluminum hats that obtained the best freezing rate from vitrification (20% dextran) was evaluated.

Sampling: One block with good vitrification of each condition was randomly chosen from the five blocks used for vitrification evaluation. From each block, a total of 10 cells were randomly selected and imaged. Five representative pictures of full cell, mitochondria, nuclei, vesicles and plasma membrane, were acquired at the magnifications of 1.2k, 8k, 10k, 12k and 20k respectively on a Hitachi H-7650 equipped with a XR41M mid mount AMT digital camera.

Criteria: Five cellular structures were analysed per cell: cytoplasm, mitochondria, nuclei, plasma membrane and vesicles. For each structure, specific criteria were defined to assess morphological preservation, as described in table 1.
To each criteria, a value of 1 or 0 was attributed, if the cellular structure followed the description or not, respectively. Hence, the maximum score was 18 and the minimum was 0. These scores were transformed in % to facilitate the analysis of the results. To all images a randomized numerical code was given to allow a non-biased evaluation. The evaluation was performed by one evaluator.

Statistical analysis: Non-parametric statistics was used to describe the data with median and interquartile range. The median of morphological preservation scores obtain in each condition were compared by applying the Mann-Whitney test. All the graphs and statistical analysis were done using the software GraphPad Prism 6.

Table 1. Criteria for the evaluation of morphological preservation

Criteria used to assess morphological preservation of cellular structures (cytoplasm, mitochondria, nuclei, vesicles and plasma membrane).

1. Cytoplasm
a. Absence of myelin figures b. Finely granular c. Homogenously distributed with no empty spaces
2. Mitochondria
a. Recognizable mitochondria b. Cristae are not ruffled c. Recognizable mitochondrial membrane d. Bilaminar structure visible with regular distance between layers e. Smooth contour
3. Nuclei
a. Recognizable nuclei b. Uniformly dense masses of condensed chromatin scattered specially surrounding the nuclear envelope and the nucleolus if visible c. Recognizable nuclear membrane d. Bilaminar structure visible with regular distance between layers e. Smooth contour
4. Vesicles
a. Recognizable vesicular membranes b. Smooth contour
5. Plasma Membrane
a. Recognizable plasma membrane b. Trilaminar structure visible with regular distance between layers c. Smooth contour

4.3.5.2 Quantification

Tested conditions: uninfected (mock) and 4, 8, 12, 16, 20 and 24 hours post-infection (PI) with IAV.

Sampling: two independent infections experiments were done. For each condition, one block was sectioned and five cells were randomly selected and imaged for quantification. To acquire the full cell, the photomontage software from FEI was used.

Criteria: the total number of single-membrane vesicles (SMV) and double-membrane vesicles (DMV) were calculated through Fiji multipoint and measure tool.

Statistical analysis: Non-parametric statistics were used to describe the data with median and interquartile range. Also, the difference of SMV and DMV medians obtained for each infection time-point was tested by applying the Kruskal-Wallis test. The multiple comparisons were tested with Dunn's test. All the graphs and statistical analysis were done using the software GraphPad Prism 6.

4.3.5.3 3D Morphological Study

Tested conditions: 16 hours PI with IAV.

Sampling: from one block, four serial sections of 120 nm were acquired. Individual single-axis tomograms were done in each section from -62º to +62º at increments of 1. The model was generated from four stacked tomograms. The tomographic reconstructions were made using the program IMOD (Kremer et al. 1996; Mastronarde 1997) and the 3D model using 3Dmod.

4.4 Immunolabeling

4.4.1 Optimization of Fixation

LM was used for immunolabeling fixation optimization (figure 7). Cells were seeded onto 13 mm glass coverslips at a density of $2.5x10^4$ cells/well in 24 well-plates and infected for 16 hours with IAV as described in section 4.2 Infection. Four different aldehydes were used for fixation. The first consisted of 4% (v/v) FA (®EMS) in 0.1 M PB and was used as a control. The other three consisted in a mixtures of 2% (v/v) FA with decreasing concentrations of GA: 0.2%, 0.1% and 0.05% (v/v) (®Polysciences) in 0.1 M PB. The fixation was performed for 2 hours, at RT. The aldehydes auto-fluorescence was blocked using 0.15% (w/v) glycine (®VWR) in PB for 10 minutes, at RT. Cells were then permeabilized with 0.2% (w/v) Triton X-100 (®Sigma Aldrich) for 7 minutes and blocked with 1% (w/v) BSA (®Sigma Aldrich) in PBS (PBS/1% BSA) for 20 minutes. Three different primary mouse antibodies (in PBS/1% BSA) were tested for 1 hour at RT: anti-calnexin (1:1000, 31290®abcam), anti-NP (1:1000, 20343®abcam) and anti-Golgi Marker (GM) 130 (1:500, 610823®BD Transduction). Cells were washed using PBS/1% BSA and subsequently incubated with anti-mouse IgG conjugated to Alexa647 (A31571®Invitrogen) and Hoechst, both diluted 1:1000 in PBS/1%BSA, for 30 minutes, RT. Coverslips were washed three times using 0.1M PB and mounted with Faramount Mounting Medium (®Dako).

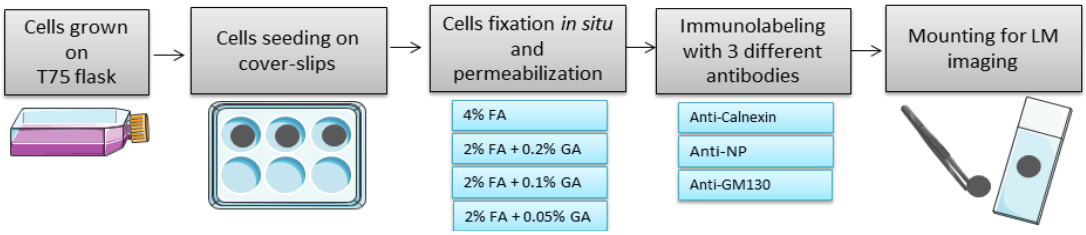

Figure 7. Scheme of immunolabeling fixation optimization

Cells were seeded in coverslips and four types of fixatives were used: 4% FA and 2% FA with 0.2%, 0.1% and 0.05% of GA. Cells were permeabilized for antibodies penetration. The fixative effect was tested in three primary antibodies: anti-calnexin, anti-NP and anti-GM130. The coverslips were mounted and imaged by LM.

4.4.2 Tokuyasu Technique

For the EM labeling cells needed to be prepared by the Tokuyasu technique (figure 8).

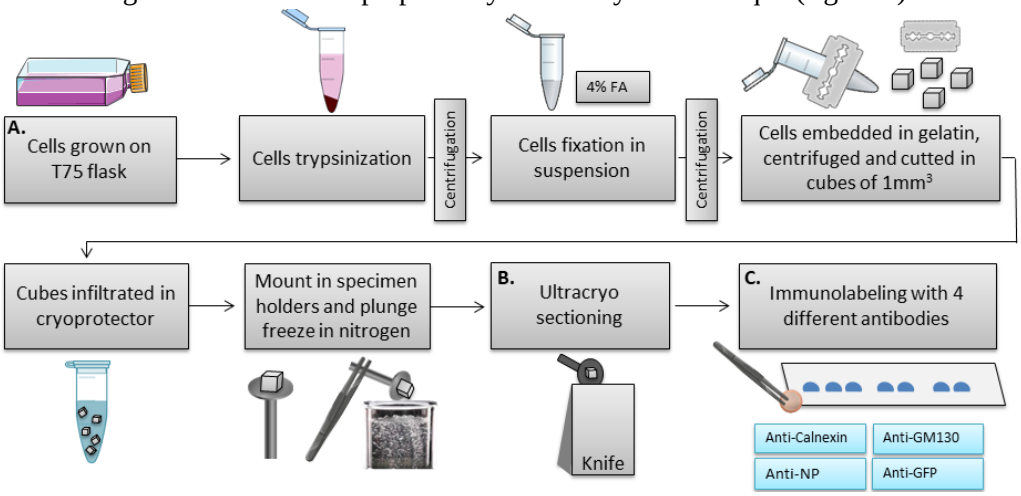

Figure 8. Scheme of Tokuyasu processing, ultracryosectioning and immunolabeling

The Tokuyasu method can be divided in three steps: processing (A.), ultracryosectioning (B.) and immunolabeling (C.). **A.** Cells were grown in culture flasks, infected and then collected through trypsinization. Fixation was performed in suspension with 4% FA. The pellet was embedded in gelatin for support and divided in $1mm^3$ cubes using a razor blade. The cell cubes were infiltrated in cryoprotector to avoid visible ice crystal formation. The specimens were then mounted in holders and frozen by immersion at-196ºC in liquid nitrogen. **B.** The frozen cubes were ultracryosectioned at -90ºC. **C.** Ultrathin sections of 50 nm were immunolabeled with four different primary antibodies: anti-calnexin, anti-NP, anti-GM130 and anti-GFP.

4.4.2.1 Processing

Sample processing is the first part of the Tokuyasu method (figure 8A). Cells were seeded onto T75 flasks at a density of $5x10^6$ cells/flask. Infection with IAV was performed for 16 hours as described in section 4.2 Infection and, later, cells were washed with PBS and trypsinized for 5 minutes. Fixation was performed in suspension using 4% (v/v) FA (®EMS) in 0.1 M PB, for 2 hours at RT. Subsequently, cells were centrifuged and washed with PB. The aldehydes were quenched using 0.15% (w/v) glycine (®VWR) in 0.1 M PB for 10 minutes at RT. Cells were infiltrated in 12% (w/v) gelatin (®Royal) for 30 minutes at 37ºC and centrifuged (1000 rcf, 5 minutes, 37ºC). The gelatin was solidified on ice, cut into 1 mm^3 cubes and placed in 2.3 M sucrose (®Alfa Aesar) in 0.1 M PB over-night (ON) at 4ºC. The cubes were mounted onto specimen holders and frozen at -196ºC by immersion into liquid nitrogen.

4.4.2.2 Ultracryomicrotomy

The second part of the Tokuyasu technique is the sectioning of the frozen samples (Figure 8B). Trimming and sectioning were performed using a Leica EM-FC7 at -90ºC. The trimming pyramid dimensions were 100x75 µm. Sections were 50 nm-thick and 0.7 M sucrose (®Alfa Aesar) in 1% (w/v) methyl-cellulose (®Sigma Aldrich) was used for picking sections from the knife onto homemade formvar-carbon coated 100-mesh grids.

4.4.2.3 Immuno-gold Labeling

The last part of the Tokuyasu method is the immunolabeling of the ultrathin sections (Figure 8C). For immunolabeling, sections were washed with PBS for 10 minutes at 37ºC to remove the pick-up solution of 0.7 M sucrose (®Alfa Aesar) in 1% (w/v) methyl-cellulose (®Sigma Aldrich). The blocking was done with PBS/1% BSA for 20 minutes at RT. Primary antibodies mouse anti-GM130, anti-calnexin, anti-NP and rabbit anti-GFP were incubated for 1 hour at RT, using a dilution of 1:25, 1:50, 1:100 and 1:500, respectively. Before incubation with the secondary detection systems, three PBS/1% BSA washes were done. Mouse primary antibodies (anti-GM130, anti-calnexin and anti-NP) were detected using goat anti-mouse IgG conjugated to 12 nm gold diluted 1:40 in PBS/1% BSA, whereas rabbit primary antibody (anti-GFP) was detected using goat anti-rabbit IgG conjugated to 18 nm gold diluted 1:20 in PBS/1% BSA. The secondary detection systems were incubated for 30 minutes at RT. Succeeding this, extensive washing with PBS was made and the gold particles were fixed by applying 1% (v/v) GA (®Polysciences) in PBS for 5 minutes at RT. Grids were washed in distilled H_2O and counterstained using methyl-cellulose–uranyl acetate solution for 5 minutes on ice.

4.4.3 Data Acquisition and Analysis

Confocal images for LM immunolabeling optimization were acquired on a Leica SP5 Live-Confocal, using a 63x 1.3 numerical aperture oil immersion objective. Images were taken at a magnification of 4.5x. For the Tokuyasu method, EM images were acquired on a Hitachi H-7650 operating at 100 keV equipped with a XR41M mid mount AMT digital camera. Fiji was used for image analysis.

4.5 Correlative Light Electron Microscopy

4.5.1 Light Microscopy

4.5.1.1 FISH on Cryostat Sections Optimization by STORM

For optimization of the FISH labeling on cryostat sections (figure 9) cells were seeded onto T75 flasks at a density of $4x10^6$ cells/flask. Cells were infected for 8 hours and, later, cells were washed with PBS and trypsinized for 5 minutes. The fixation was performed in suspension using 4% (v/v) FA (®EMS)

in 0.1 M PB, for 10 minutes at RT. Cells were centrifuged and washed three times with PB. The aldehydes were quenched using 0.15% (w/v) glycine (®VWR) in 0.1 M PB for 10 minutes at RT. After this time, the cells were infiltrated in 2% (w/v) agarose (®OmniPur) for 15 minutes at 37ºC and centrifuged (1000 rcf, 5 minutes, 37ºC). The agarose was solidified on ice and placed in 30% (w/v) sucrose (®Alfa Aesar), ON at 4ºC. The agarose blocks were embedded in optimal cutting temperature compound (OCT) (®Sakura) and frozen at -196ºC by immersion into liquid nitrogen. 10 µm sections were obtained using a Leica Cryostat CM3050S and placed in coordinated cover-slips with or without coating of 2% (v/v) (3-Aminopropyl)triethoxysilane (APES) (®Sigma Aldrich) in acetone. For the FISH labeling cells were incubated in 2x SSC (®Fisher Scientific) containing 40% formamide (®Sigma Aldrich), 0.01M EDTA (®Acros Organics), 35mM NaH_2PO_4 (®Amresco), 5% Dextran Sulphate (®Alfa Aesar) and 250ng/ml tRNA for 1 hour at 37ºC in the dark. Different vRNA probes, produced as described previously (Amorim et al. 2011), were used to detect: segment 2 - PB1 labelled with Cy5 and segment 1 - PB2 labelled with Cy3. These probes were diluted 1:200 in hybridization solution, boiled for 5 minutes and immediately placed on ice. Ribolock (®Roche) was added to this mixture in a dilution of 1:400. The probes were incubated for 16 hours at 37ºC, in the dark. Samples were washed in hybridization buffer twice for 15 minutes at 37ºC, followed by three washes in PBS, RT. The nuclei were stained using Hoechst at a dilution of 1:1000, for 10 minutes, RT. To finish cells were washed in PBS. Before STORM acquisitions, samples were mounted using imaging buffer composed by 11% (v/v) mercaptoethylamine (made from stock solution of 7.7% cysteamine (®Sigma Aldrich) in Hydrochloric Acid 360 mM), 11% (w/v) glucose oxidase (®Sigma Aldrich), 2% oxygen scavenger (made from stock solution of 7% (w/v) glucose oxidase (®Sigma Aldrich) and 25% (v/v) catalase in Tris buffer pH8) and 2% cyclooctatetraene (®Sigma Aldrich) in PBS. The coverslips were sealed using twinsil (®Picodent).

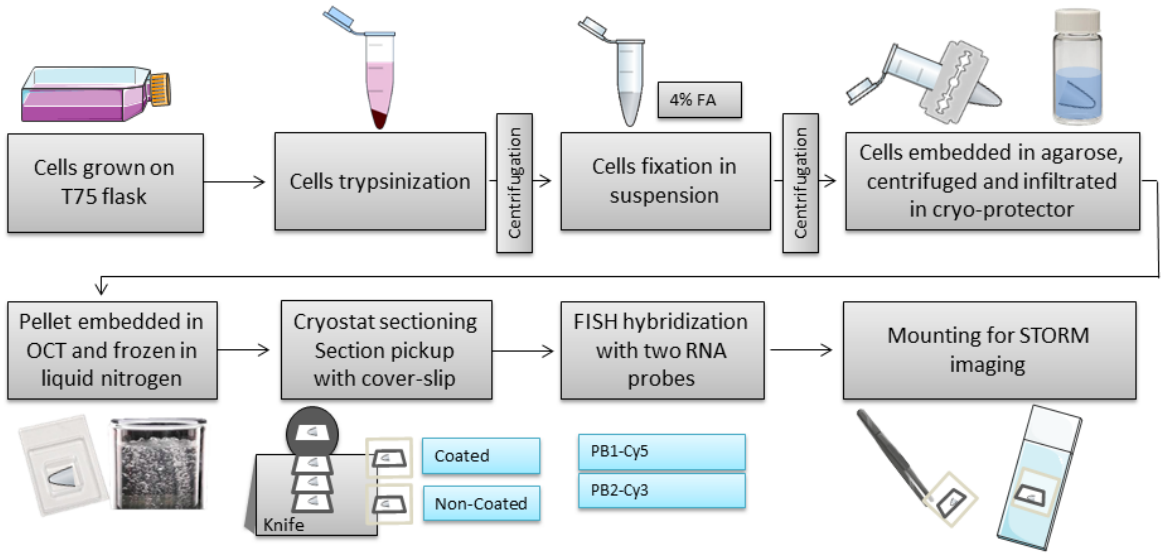

Figure 9. Scheme of FISH on Cryostat Sections

For FISH on cryostat sections, cells were trypsinized and fixed in suspension with 4% FA. Cells were then pelleted and embedded in agarose for support. The agarose pellet was infiltrated in cryo-protector and embedded in OCT before freezing at -196ºC in liquid nitrogen. After processing, sections were cut using a cryostat. Two types of cover-slips were tested for sections pickup: coated and non-coated. FISH was performed on sections with two RNA probes: PB1-Cy5 and PB2-Cy3. Cover-slips were mounted only before acquisition with imaging buffer.

4.5.2 Electron Microscopy

4.5.2.1 Processing

For EM processing, the cryostat sections were washed 10 times with 0.1M PB and post-fixed in 1% (v/v) osmium tetroxide (®EMS) with 1% (w/v) potassium ferrocyanide (®Sigma Aldrich) in 0.1 M

PB for 30 minutes, on ice. Sections were washed twice for 5 minutes in 0.1M PB and twice in distilled H_2O. The dehydration was performed in a graded ethanol series of 30%, 50%, 75%, 90% and 100%, for 10 minutes each. Embed-812 epoxy resin (®EMS) was used for embedding and hardened ON at 60ºC.

4.5.2.2 Targeted Ultramicrotomy and Post-Staining

For CLEM, the exact same cell image acquired by LM needs to be tracked in the EM resin block. This can be achieved using a coverslip carved with a coordinated grid that can be seen in LM and that will also be imprinted in the resin block (Figure 10). The exact coordinate was then targeted for trimming and sectioned using a Leica UC7. After sectioning, the grids containing the sections were stained as previously described in the section 4.3.3 - Ultramicrotomy and Post-Staining.

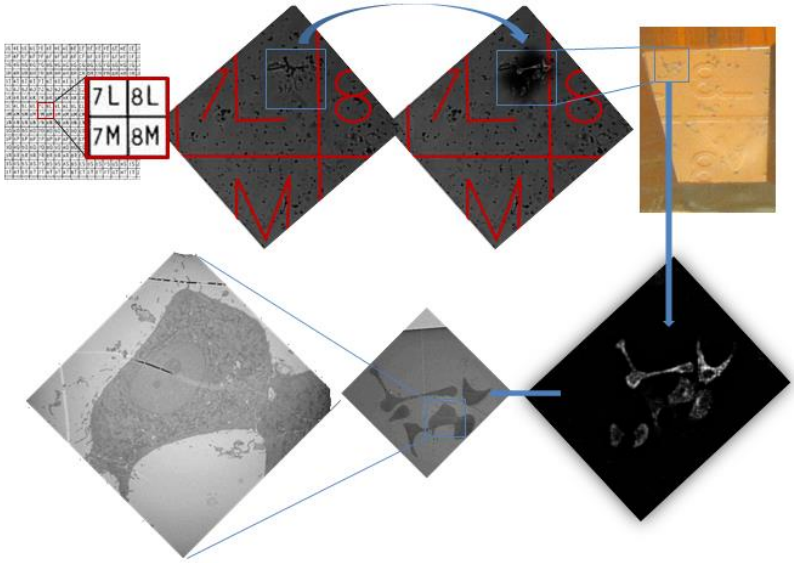

Figure 10. Scheme of coordinate system for targeted ultramicrotomy

The coordinated pattern underneath the region of interest is imaged in LM. Later, after embedding, the pattern imprinted in the resin block is targeted, trimmed and sectioned. The same region imaged in LM can be imaged in EM.

4.5.3 Data Acquisition and Analysis

Super-resolution images were acquired on a Nikon ECLIPSE TI, using a 100x 1.45 numerical aperture oil immersion objective and a Hamamatsu ORCA Flash 4.0 camera. The STORM acquisition with the red laser Cy5 was done at 110 mW and with the green Cy3 at 80 mW with an exposure time of 10 ms in 20,000 images. EM images were acquired on a Hitachi H-7650 operating at 100 keV equipped with a XR41M mid mount AMT digital camera. Fiji was used for the STORM reconstructions.

5. Results

"Chance favors the prepared mind" – Louis Pasteur

5.1 High Pressure Freezing – Freeze Substitution Technique Optimization

For the optimization of HPF-FS technique two parameters were evaluated: vitrification rate and morphological preservation. Both parameters are affected by the type of specimen carrier and filler chosen for loading and freezing, which need to be carefully selected according to the specimen type and biological question.

5.1.1 Vitrification Evaluation

Vitrification refers to the process of transformation from a liquid to a solid without crystallization. If cells are not properly vitrified during HPF-FS ice damage will occur. For evaluation of the vitrification rate aluminum hats and aclar flat disks were tested. The first used three types of cryo-protectants: 1-hexadecene, 20% (w/v) dextran and 20% (w/v) BSA. The second used only 1-hexadecene due to the reduced thickness. The cells were evaluated as vitrified if no crystallization patterns were detected (figure 11A). One cell per block was analysed in a total of five cells per condition (n = 5) and the results are presented as blocks. The number of blocks was averaged for each tested condition and plotted as the % of vitrified blocks (figure 11B).

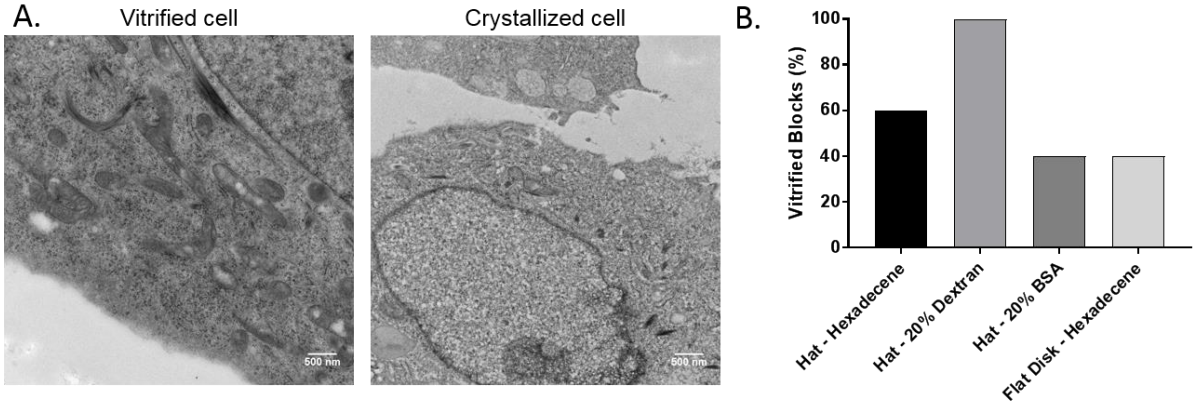

Figure 11. Vitrification evaluation

Vitrification was determined by the absence of crystallization patterns in the cells. **A.** Example of vitrified and crystallized cells. The first exhibit a homogenous cytoplasm and nuclei while the other present a network of empty spaces created by the ice crystals. **B.** The number of vitrified blocks was calculated through the evaluation of crystallization patterns in the analysed cell of each block. Five cells were evaluated per condition (n = 5) and the results are present as % of vitrified blocks. The results indicate that the best vitrification rate was acquired with the combination of hats with 20% dextran.

The best vitrification rate was achieved with the aluminum hats frozen with 20% dextran, where all analysed blocks showed vitrified cells. In general, all the conditions using hats had equal or better vitrification rates than flat disks. The combination hats with 1-hexadecene and 20% BSA achieved 60 and 40% vitrification rate, respectively. In the condition flat disk with 1-hexadecene only 40% of the blocks were vitrified.

5.1.2 Morphological Preservation

The analysis of morphological preservation was made in two conditions: hats and flat disks (figure 12 A and B, respectively). Both types of holders were evaluated since they request a different sample preparation for loading that can affect the ultrastructure preservation. In the hats, only the blocks frozen with 20% dextran were considered since it obtained the best vitrification rate. For each analyzed condition, one block with good vitrification was randomly chosen and 10 cells were imaged per condition (n = 10). The morphological preservation was assessed by evaluating the ultrastructural maintenance of five cellular structures (cytoplasm, mitochondria, nuclei, plasma membrane and vesicles) as described in the table 1 of the material and methods section. Representative images of each of the conditions evaluated are shown in figure 12C.

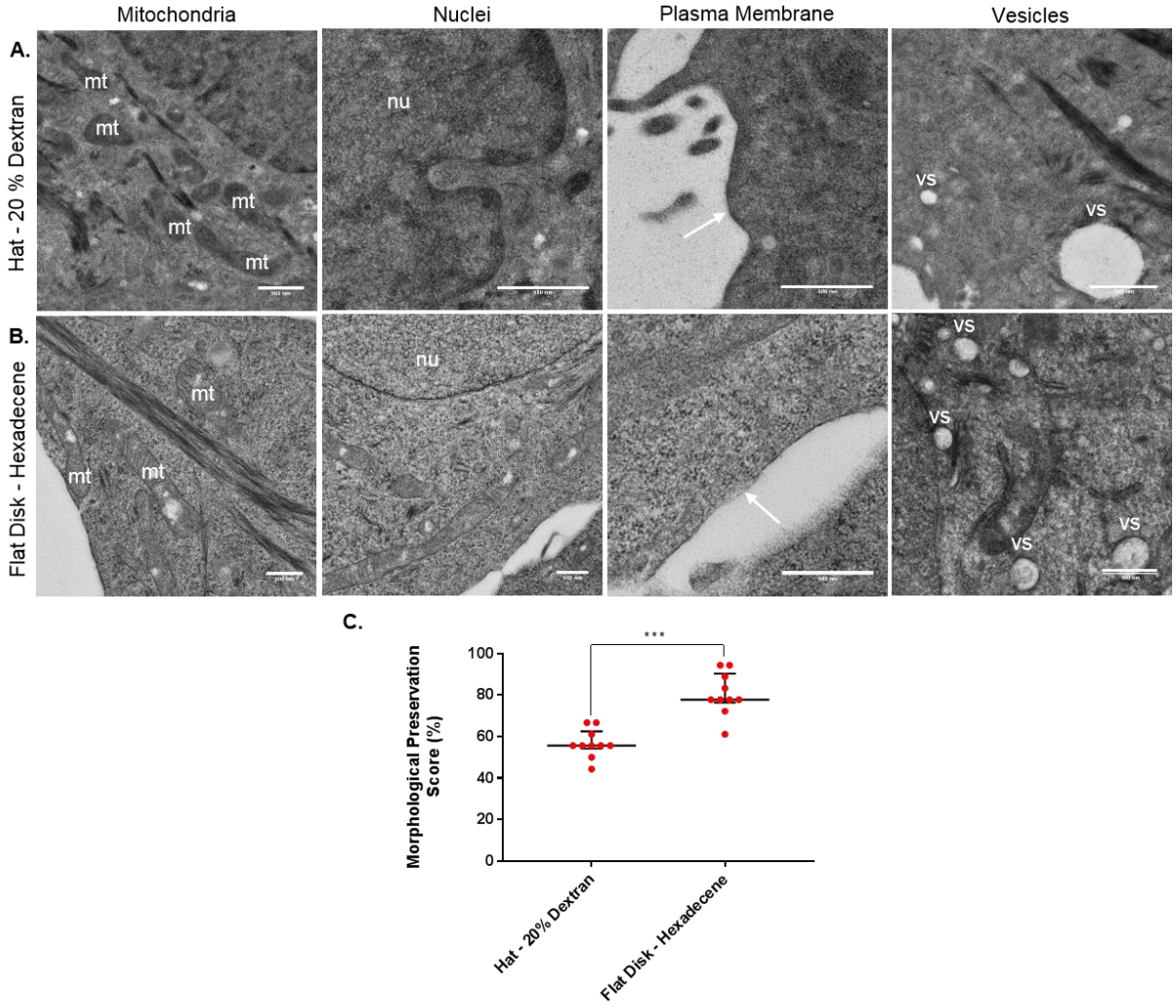

Figure 12. Analysis of morphological preservation of the cell ultrastructure

The morphological preservation of the cell cytoplasm, nuclei (represented as nu), mitochondria (represented as mt), vesicles (represented as vs) and plasma membrane (white arrow) was analysed by TEM. Representative images of the ultrastructural features in cells frozen using: **A.** Hats and 20% dextran and **B.** Flat disks and hexadecene. One cell of each block was analysed per condition. Bar = 500 nm. Images acquired on a Hitachi H-7650 operating at 100 keV and analysed by the software Fiji. **C.** The morphological preservation score was calculated through the ultrastructural evaluation of the cytoplasm, nuclei, plasma membrane, mitochondria and vesicles, using a set of criteria defined in Table 1 of material and methods section. Hats with 20% dextran obtained a median value score of 55.6% and flat disk with hexadecene 77.8%. Ten cells were analysed per condition (n=10). Error bars represent interquartile range. Statistical significance was determined by Mann-Whitney test. A p value < 0.001 (***) was considered statistically significant. The graph and statistical analysis were done using the software GraphPad Prism 6.

The cytoplasm presented no empty spaces or clumping of ribosomes in both conditions. Also, no myelin figures characteristic of the chemical fixation were detected. It is possible to see that the cytoplasm is finely granular (stippled) only in the cells frozen with hats. Membranes of flat disks condition but not hats, are smooth and not distorted. Also in the hats, the mitochondria presented collapsed internal and external membranes. The vesicular membranes appear to be better preserved in the flat disks than in the hats.

The cells frozen with hats and 20% dextran obtained a median morphological preservation score of 55.6% and the ones frozen with flat disk with hexadecene attained 77.8%. The difference between medians was tested by the Mann-Whitney test and p value inferior to 0.001 allowed this difference to be accepted and to state that flat disk condition allows a better morphological preservation.

5.2 Characterization of IAV induced Vesicular Clustering

Many viruses modify host cell membranes to facilitate their own replication. This is widely studied in positive sense RNA viruses, in which rearrangements lead to many distinct morphological features, ranging from convoluted membranes to spherule structures and double membrane vesicles (DMV).

Several questions arise from observing how viruses sculpture membrane architecture: which membranes are modified and what are the morphological features of such modifications? What is the role of these structures in infection? The answer to these questions is important because it contribute to a better knowledge of the viral lifecycles which can ultimately lead to prevention of pathogenic viral infections by the development of antiviral drugs. To answer some of these questions, the characteristics of clustered vesicles induced by IAV over the course of infection were evaluated through quantification of vesicle number, analysis of the morphological features and immunolabeling.

5.2.1 Quantification of Vesicle Number during IAV Infection

Optimization of HPF-FS technique led to the conclusion that the best freezing protocol included flat disks frozen with hexadecene. Hence, IAV infected cells were processed accordingly. Quantification of the number of vesicles composed of either a single or a double membrane (SMV or DMV) was made by visual inspection photomontages of 10 randomly chosen cells per condition (n = 10) from two independent experiments (figure 13). For the identification and calculation of the vesicular number the software Fiji multipoint and measure tool was used.

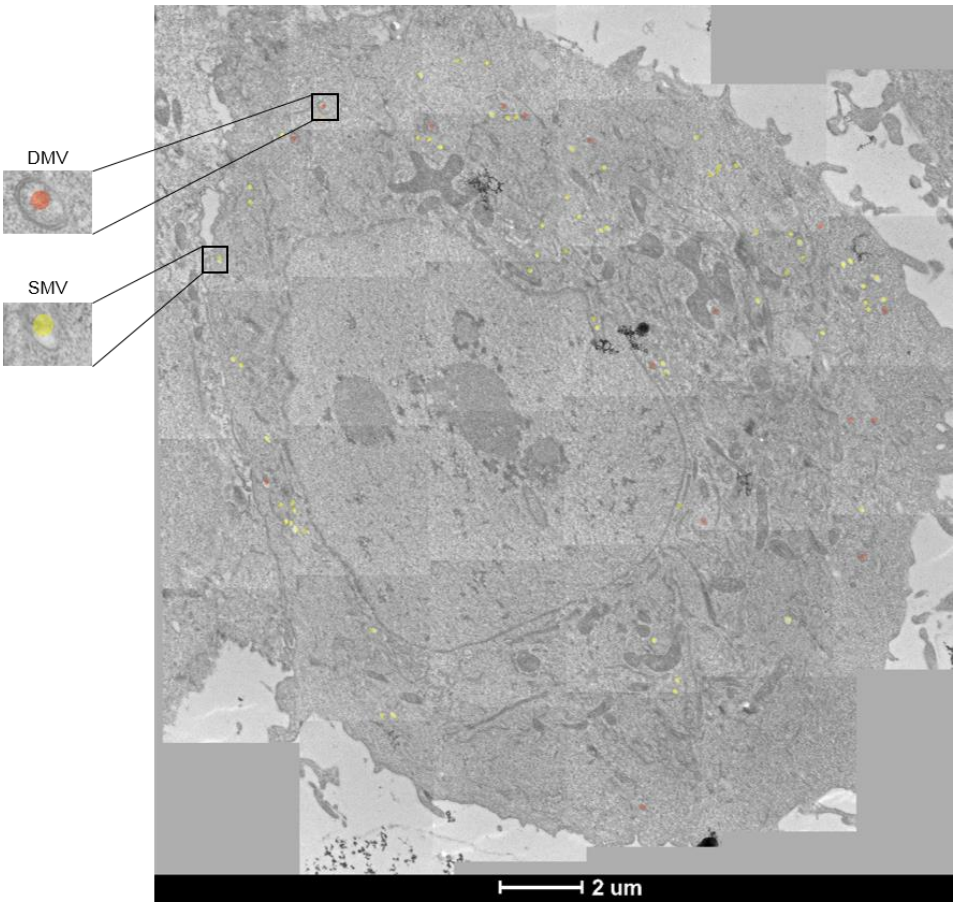

Figure 13. Photomontage for the quantification of vesicles number

The number of SMVs (yellow circle) and DMVs (orange circle) was counted in IAV infected and mock cells. Cellular photomontages were acquired on a FEI Tecnai G^2 Spirit BioTWIN operating at 120 keV and the calculation of the vesicular number was done by the software Fiji multipoint and measure tool. Bar = 2 µm.

Within clusters, the SMVs were clearly prevalent. Median number of vesicles per cell increased from 18-24 in mock and 4 hours PI to 123-168 from 8 to 24 hours PI (figure 14). The increase was observed at the time that corresponded to vRNP translocation from the nucleus to the cytoplasm. This increase was not statistically different very likely as a consequence of the low number of cells analysed and inter cell variation.

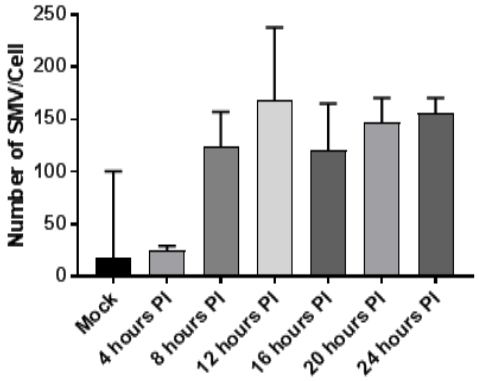

Figure 14. Quantification of SMV in mock, 4, 8, 12, 16, 20 and 24 hours PI with IAV

The total number of SMV was counted in ten individual cells per condition (n = 10) from two independent IAV infection experiments. The SMV median value was 18, 24, 123, 168, 121, 147 and 156 for mock, 4, 8, 12, 16, 20 and 24 hours PI, respectively. Error bars represent interquartile range. Statistical significance was determined by Kruskal-Wallis test and the multiple comparisons were later tested by Dunn's test. A p value >0.05 was considered statistically non-significant.

The increase in DMVs was modest, ranging from 0 in mock and 4 hours PI to a maximum of 7 from 8 to 24 hours PI (figure 15). The median differences were tested by applying the same statistical tests as in the SMV, described above. A p value of 0.011 and 0.014 between the conditions mock and 12 hours PI and mock and 16 hours PI allows us to accept that there is a difference between the medians of these conditions. Although with a modest increase, DMVs persistently appear during IAV infection, strongly indication that these are a consistent event in infection. However, the role played in infection remains unclear.

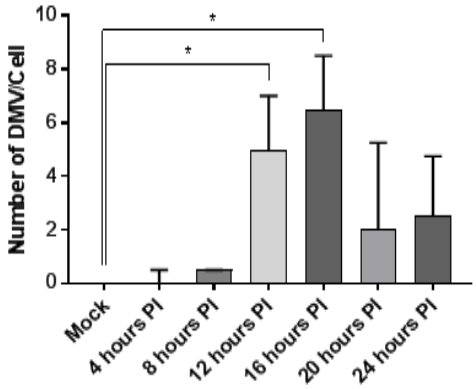

Figure 15. Quantification of DMV in mock, 4, 8, 12, 16, 20 and 24 hours PI with IAV

The total number of DMV was counted in ten individual cells per condition (n = 10) from two independent IAV infection experiments. The DMV median value was 0, 0, 1, 5, 7, 2 and 3 for mock, 4, 8, 12, 16, 20 and 24 hours PI, respectively. Error bars represent interquartile range. Statistical significance was determined by Kruskal-Wallis test and the multiple comparisons were later tested by Dunn's test. A p value <0.05 (*) was considered statistically significant between the conditions mock and 12 hours PI and mock and 16 hours PI.

5.2.2 Vesicles Morphological Study

To determine the environment in which SMV and DMV can be found, and to assess the origin of these membranes, a morphological study was done by TEM at 16 hours PI in cells infected with IAV. This time-point was chosen based on the highest number of DMVs found. From one block, four serial sections of 120 nm were acquired. The SMVs observed were composed by a single bilayer, while the DMVs were composed by two distinguishable and concentric bilayers (figure 16).

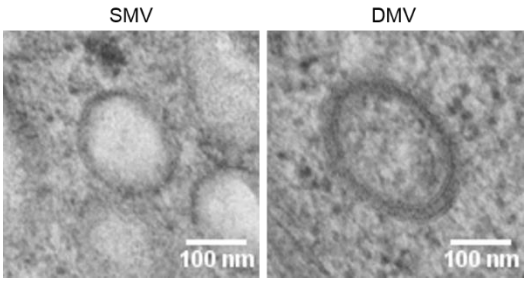

Figure 16. SMV and DMV morphology at 16 hours PI with IAV

A morphological study was done in cells infected with IAV for 16 hours. Serial sections of 120 nm from one block (n = 1) were inspected by TEM. SMVs presented only one bilayer and DMVs had two concentric bilayers. Bar = 100 nm. Images acquired on a FEI Tecnai G^2 Spirit BioTWIN operating at 120 keV and analysed by the software Fiji.

A tomographic and 3D study was done, from the four serial sections. In the same area of each section, four single-axis tomograms were acquired, stacked and reconstructed to produce the tomographic slices and a 3D model (figure 17 and 18, respectively).

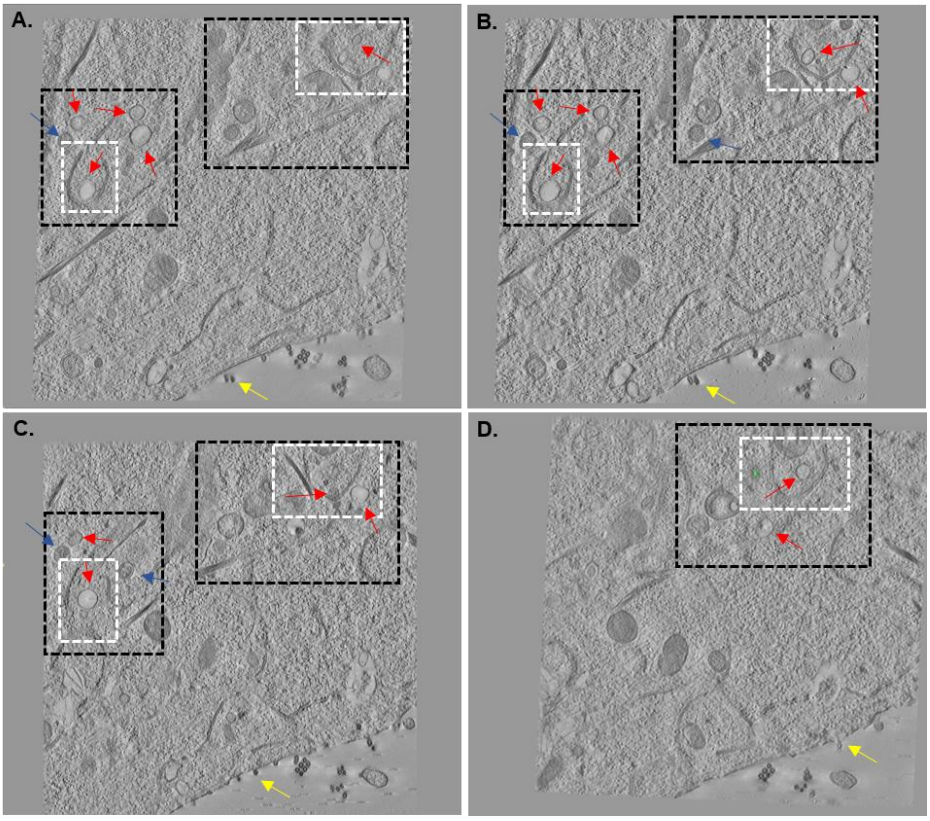

Figure 17. Serial slices through single-axis tomograms of a 16 hours IAV infected cell

To study in detail the environment in which SMVs and DMVs can be found, a tomography study was carried in a 16 hours IAV infected cell. Four tomograms were acquired, stacked and reconstructed from the same area in four serial sections of 120 nm. **A; B; C;** and **D.** represent serial slices through the final reconstructed tomogram. The tomograms were acquired on a FEI Tecnai G^2 Spirit BioTWIN operating at 120 keV and the reconstruction was done using IMOD
It is possible to note that both types of vesicles appear in the clusters (black dashed boxes) and near the ER. Indeed, SMVs (red arrows) appear wrapped in ER membranes (white dashed box) while DMVs (blue arrows) seem to be outside of this structure. At the plasma membrane IAV virions are visible (yellow arrows).

In these images two regions of clustered vesicles (black dashed boxes) are present. Both regions present the normal dominance of SMV however also DMVs appeared as indicated by the blue arrows (figure 17). The detailed analysis of the ultrastructural vesicular context suggests that SMVs appear in close proximity to ER membranes and in some cases seem to be wrapped by these membranes (white dashed boxes). On the other hand, the DMVs appear near the ER, in the cytoplasm and close to the plasma membrane, but not surrounded by it.

The involvement of the ER membranes in the viral lifecycle was already described for many distinct positive sense RNA viruses, such as Flaviviruses, Coronaviruses and Picornaviruses. The results described for IAV are consistent with what has been shown for the Picornaviruses in which SMVs flatten, to give rise to DMVs.

A representative tomogram slice is depicted together with the 3D model reconstructed from the stacked tomograms (figure 18).

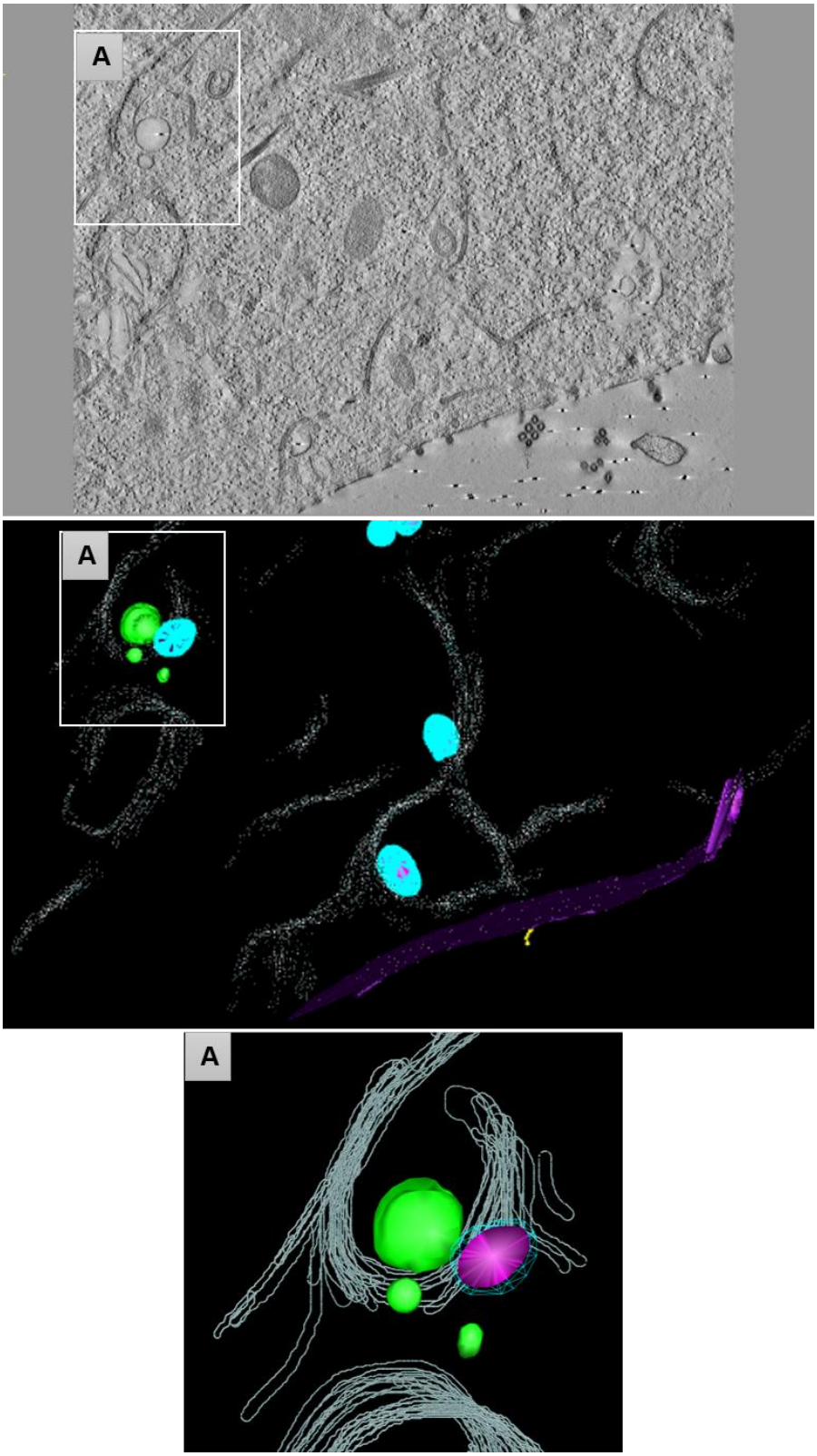

Figure 18. 3D model of SMVs and DMVs of a 16 hours IAV infected cell

From the four serial sections acquired from a 16 hours IAV PI cell, four single-axis tomograms were acquired, stacked and reconstructed (top image). The tomographic reconstruction was modelled to generate the 3D data (middle image). SMVs are represented in green, DMVs outer membrane as a mesh in light blue and the inner membrane in pink. Plasma membrane is showed in purple and ER as white lines. It was possible to detect the SMV and DMV structures in close connection with the ER (box A). **A.** SMV wrapped in ER membranes and DMV in the outside of the structure.

5.2.3 Clustered Structures Origin and Cellular Context

Immunolabeling was used to confirm the cellular context in which SMV and DMV can be found. Four markers were used: GM130 protein for the Golgi membranes, calnexin for the ER membranes, viral NP protein for the virus genome and GFP for the GFP-Rab11. Golgi and ER markers were included since they are both involved in the post-translational processing of the viral envelope proteins NA, HA and M2. Moreover, a close proximity was found between SMVs and the ER during the morphologic studies. The Rab11 marker was tested to confirm if SMVs and DMVs were in fact ERC membranes. Finally, the viral marker NP was used to test if the SMVs and/or DMVs were used for viral genome trafficking.

5.2.3.1 Immunolabeling Optimization

To be able to label all the markers for EM, an optimization of the fixation conditions was necessary and made by LM. The fixation with only FA is the gold-standard fixation for immunolabeling; however GA is usually present to preserve the morphology at the EM level. A balance between ultrastructure and immunoreactivity needed to be found since GA can hinder the immunoreactivity of certain antigens. Therefore, in cells infected with IAV for 16 hours, the four markers: GM130, calnexin, NP and GFP-Rab11, were studied for the capability to maintain its immunoreactivity in different fixation conditions. The first three, through detection with the secondary antibody Alexa647 and the last one directly by GFP endogenous expression. The following fixatives were tested: 2% FA with 0.2%, 0.1% and 0.05% GA. As a control, the reference fixative 4% FA was included in the test (figure 19).

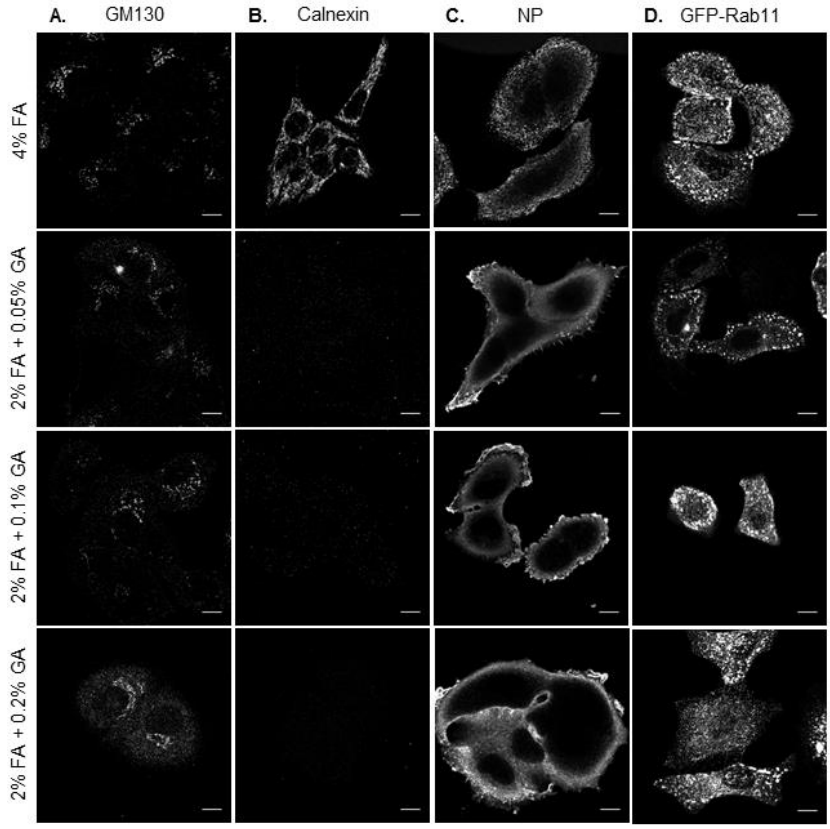

Figure 19. Fixatives testing for GM130, calnexin, NP and GFP-Rab11 detection

The immunoreactivity of GM130, calnexin, NP and GFP-Rab11 was tested using fixative mixtures with and without GA. **A.** GM130 marker immunoreactivity was the same with all four fixatives. **B.** The calnexin signal was hindered by the mixtures with GA and only with just 4% FA signal was detected. **C.** The fixatives with GA altered the localization of NP. This is possible to see through a strong detection at the periphery but not in the centre of the cell. **D.** The GFP-Rab11 signal was not affected even with higher GA concentrations. Bar = 10µm. Images acquired on a Leica SP5 Live Confocal, using a 63x 1.3 numerical aperture oil immersion objective and analysed by the software Fiji.

The GM130 signal was possible to visualize in all the aldehyde mixtures (figure 19A). The presence of GA did not affect the labeling of GM130, even at highest concentration tested. The same did not happen when detecting calnexin. The inclusion of GA in the fixative completely abolished calnexin signal, which can be clearly observed when 4% FA is used (figure 19B). The NP staining was also affected by the usage of GA, being strongly detected at the cellular periphery with no vesicular aggregation in cytosol (figure 19C), as seen in the control 4% FA. It was also possible to state an alteration of the NP localization with GA fixation. The GFP-Rab11 signal was maintained, regardless of the GA concentration used. Strong Rab11 vesicles can be observed scattered through the cytoplasm (figure 19D).

5.2.3.2 Immuno-gold Labeling for Electron Microscopy

Optimization of the fixation conditions for immunolabeling led to the conclusion that 4% FA was the best fixative to detect all markers. Cells infected for 16 hours with IAV, were fixed with 4% FA and further processed for immuno-gold labeling. The ultrastructural analysis showed that vesicular ultrastructure was not affected by the lack of GA in the primary fixation and that it was possible to differentiate between SMVs and DMVs (figure 20).

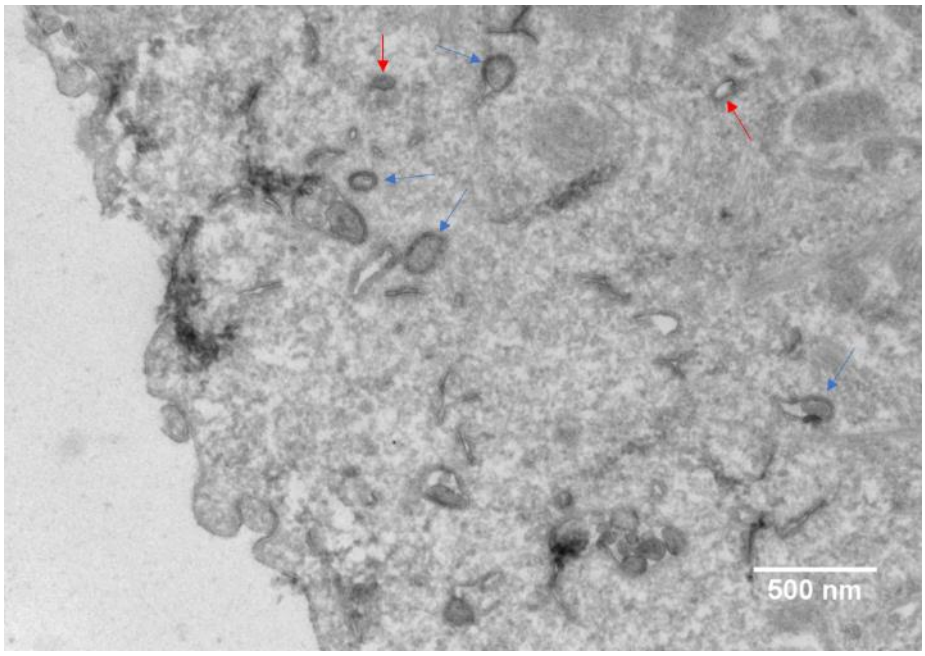

Figure 20. Ultrastructural analysis of a 16 hour IAV infected cell fixed with 4% FA

The vesicles (arrows) ultrastructure in a 16 hours IAV infected cell fixed with 4% FA for immuno-gold labeling was not affected. The membranes are preserved and enable to distinguish between SMVs (red arrows) and DMVs (blue arrows).
Bar = 500 nm. Images acquired on a Hitachi H-7650 operating at 100 keV and analysed by the software Fiji.

To detect the markers in EM sections, secondary antibodies coupled to gold particles were used. Primary mouse antibodies against GM130, calnexin and NP were detected with IgG-Gold 12 nm, and rabbit antibodies GFP with IgG-Gold 18 nm (figure 21). The labeling of Golgi and ER (figure 21 A and B, respectively), was very poor, with few positive markers detected. In both cases sparse gold particles were found, which can correspond to Golgi and ER (orange and green arrow in the figure 21 A and B, respectively). No conclusions can be drawn in relation to the abundance of membranes found in close proximity to clustered vesicles. Conversely, the staining for NP and GFP (Rab11) was strong in the vesicles present in clusters, showing clearly an association between the clusters, IAV genome and the ERC. Particularly in the GFP (Rab11) labeling, membranes clustered in the cytosol are

strongly decorated with gold particles (figure 21D). Also, NP labeling is observed in regions of clustered vesicles and match electron dense features in between vesicular aggregates (figure 21C).

Mock cells were used as a negative control and GFP labeling is detected sparsely distributed in the cytosol (as predicted) whilst NP is not detected. Additionally, a primary negative control was used for the secondary IgG-Gold 12 and 18 nm detection systems and no particles were detected. Thus, no unspecific binding occurred in this immunolabeling (figure 21 E and F, respectively).

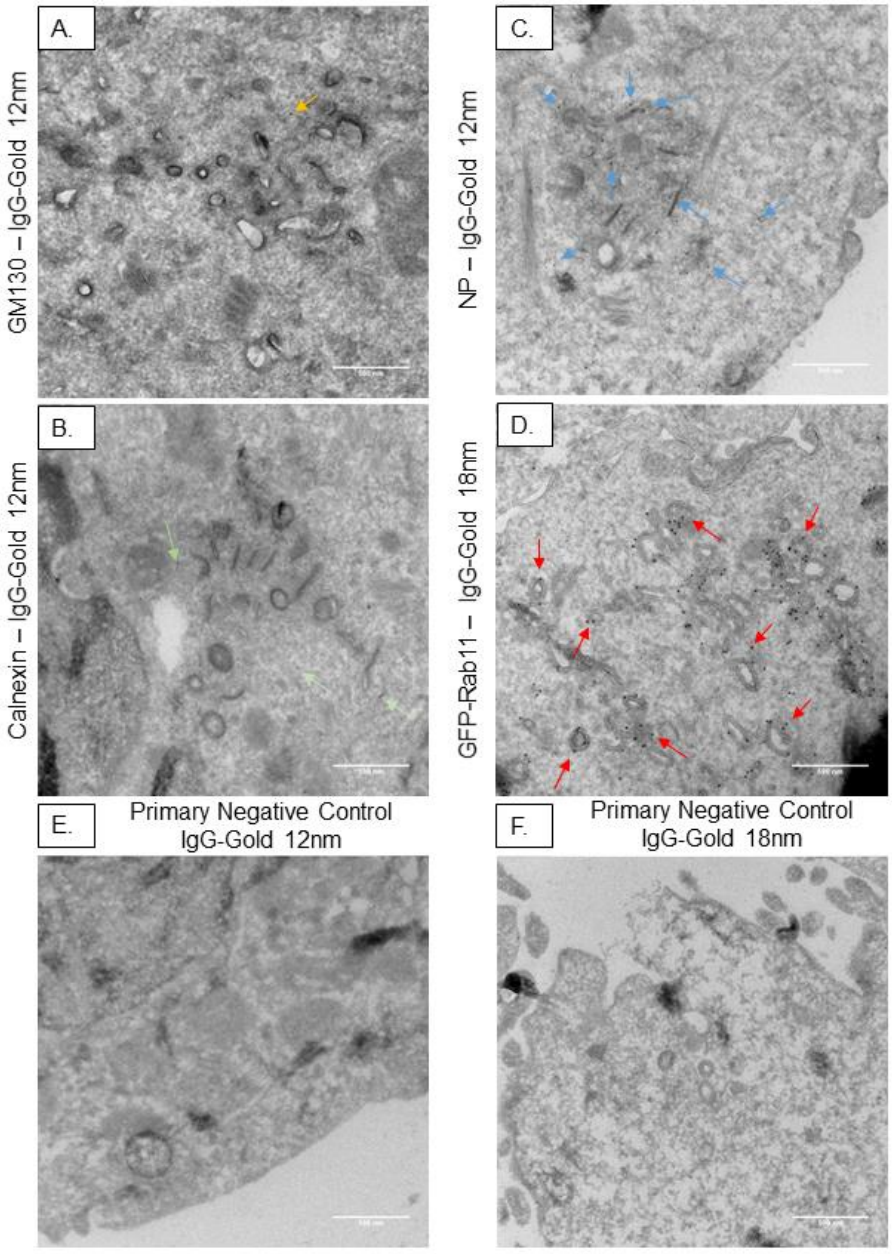

Figure 21. Immuno-gold labeling of GM130, calnexin, NP and GFP-Rab11

To determine the membranous environment in the vicinity of clusters, immuno-gold labelling was performed with markers for different organelles. **A.** GM130 (Golgi) detection with IgG-gold of 12nm. No labeling was detected associated with the clusters. Although modest cytoplasmic labeling was detected (orange arrow) **B.** Calnexin (ER), labeling was not detected in the vicinity of clusters. Some labeling was found associated with ER (green arrows), but again in modest amounts. **C.** NP (IAV viral genome) was detected within the clusters (blue arrows). **D.** GFP (GFP-Rab11, ERC) was detected strongly in clustered membranes (red arrows). **E.** and **F.** Secondary gold antibodies are specific and in the absence of primary antibodies no labeling was detected. Bar = 500 nm. Images acquired on a Hitachi H-7650 operating at 100 keV and analysed by the software Fiji.

A closer and more detailed analysis revealed that both SMVs (red arrows) and DMVs (blue arrows) were labeled with GFP (to detected GFP-Rab11) and NP (to detected IAV genome) (figure 22). This shows that both types of vesicles originate at the ERC and are loaded with vRNPs.

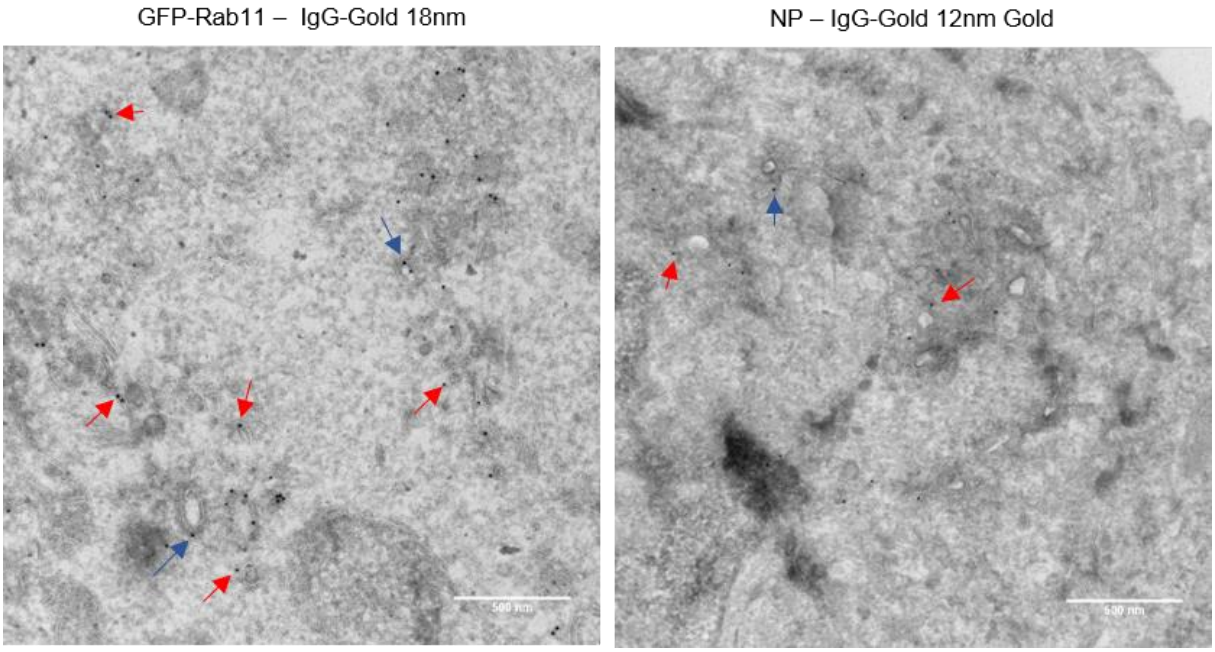

Figure 22. SMVs and DMVs label with GFP-Rab11 and NP

Immuno detection of NP with IgG-gold of 12nm and GFP-Rab11 of 18nm gave the possibility to see that both SMVs (red arrows) and DMVs (blue arrows) label with NP and GFP-Rab11 markers. Bar = 500 nm. Images acquired on a Hitachi H-7650 operating at 100 keV and analysed by the software Fiji.

5.2.4 CLEM Method Development – FISH, STORM and EM

Published data resulting from this work, evidenced the involvement of ERC membranes in the trafficking of IAV genome and showed that vesicles clustered as a result of infection. This allowed to propose a model in which vesicular clustering operates upstream genome assembly (Vale-Costa et al. 2016). This model is in opposition with another recently hypothesized in which IAV genome assembly occurred *en route* to the plasma membrane via collision of vesicles (Lakdawala et al. 2014; Chou et al. 2013). The latter model was supported by experiments using super resolution microscopy to match two and four distinct vRNPs in the cytosol (Lakdawala et al. 2014; Chou et al. 2013).

In this work, I tried to establish a method with higher resolving power - CLEM combining FISH, STORM and EM. This method allows to observe specific vRNPs, detected in areas of clustered vesicles and understand if genomic complex formation could be resolved.

5.2.4.1 FISH on Cryostat Sections for STORM

The first challenge was to permeabilize cells in order to allow the entry and hybridization of FISH probes. Chemical permeabilization destroys the ultrastructural features and so, the alternative is to physically permeabilize the cells through sectioning, for example using a cryostat.

Although FISH on cryostat sections is a common approach ADD BANCROFT, some points needed to be adapted for the subsequent STORM imaging and EM processing, namely the section support. This support was optimized according to specific criteria: 1) permit LM imaging; 2) be resistant and non-

reactive to chemicals used for EM processing; and 3) hold in place the section during LM imaging and EM processing, but be detachable from the resin after embedding.

Glass slides could not be used since they do not easily detach from the resin block after embedding. The slide easily breaks leaving traces of glass in the block, thus obstructing the sectioning. For this reason, coverslips were chosen and tested with or without coating with 2% APES in acetone, which rises the adherence of section to the support (Maddox & Jenkins 1987).

Both tested coverslips, enable LM imaging however, the non-coated coverslips lost the sections during the long incubations of FISH. Coverslips with coating were resistant to all the procedures, hold the section on place and detached easily from the resin block.

Furthermore, the FISH protocol also needed testing on cryostat sections to be imaged for STORM. The specificity of the FISH protocol was confirmed by labeling both mock and 8 hours IAV infected cells, with two distinct probes, Cy3-PB2 and Cy5-PB1 (figure 23).

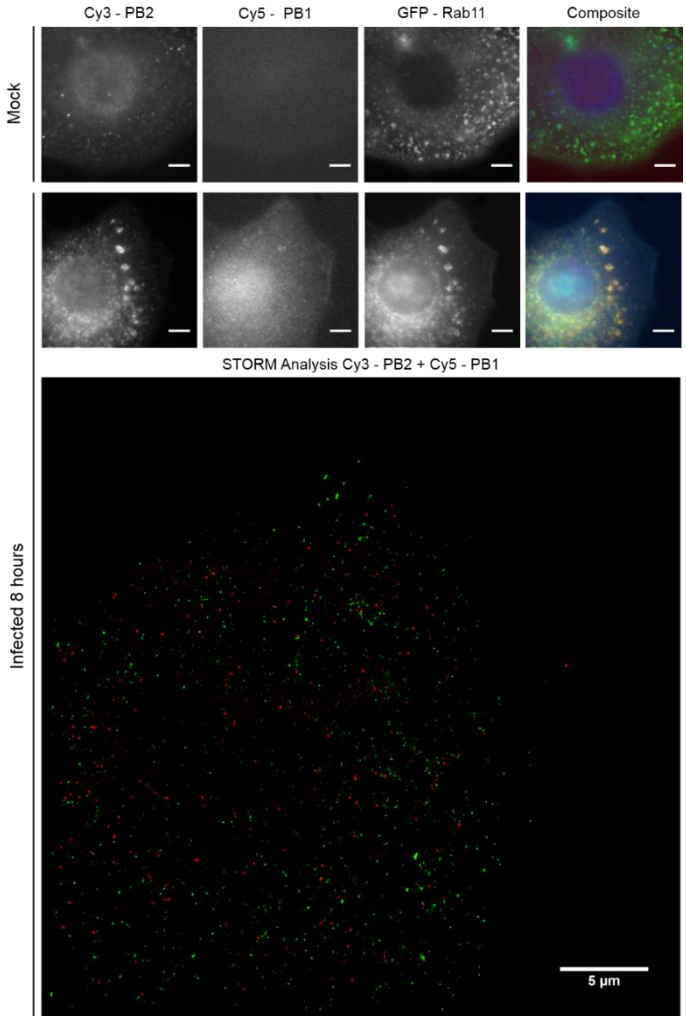

Figure 23. FISH on cryostat sections of cells uninfected and infected for 8 hours with IAV

The FISH protocol was tested in cryostat sections, using two probes Cy3-PB2 and Cy5-PB1 on GFP-Rab11 cells that where infected or not with IAV for 8 hours. It is visible the intense labeling on the infected cells and the correlation with the GFP-Rab11 signal. In the mock cells the signal is almost absent. The STORM reconstructrion shows Cy3.PB2 in green and Cy5-PB1 in red, but unfortunately the reconstruction is very poor and needs additional troubleshooting. Bar = 5 µm. Images acquired on a Nikon ECLIPSE TI, using a 100x 1.45 numerical aperture oil immersion objective and analysed by the software Fiji. The STORM acquisition with the red laser Cy5 was done at 110 mW and with the green Cy3 at 80 mW with an exposure time of 10 ms in 20,000 images.

Reduced unspecific background labeling was detected in mock cells with both probes. The background becomes negligible when compared to the specific labeling of infected cells, where accumulation of PB2 and PB1 is visible in the clusters of GFP-Rab11. Interestingly, the cryostat sections do not withstand the STORM imaging buffer for long periods. The image acquisition needs to be done in a maximum window of approximately 15 minutes. The STORM reconstruction show PB2 (in green) and the PB1 (in red) spread in the cytoplasm but further controls swill be needed to confirm if indeed vRNPs are being properly detected.

5.2.4.2 Electron Microscopy Processing

Given that it was possible to acquire LM images of FISH labeling in cryostat sections, these were further processed for EM. Damage in the ultrastructure was expected, caused by long incubations with chemicals used for FISH (formamide) and STORM imaging buffer. Severe extraction of the cytoplasm could be observed, yet it is possible to conserve the ultrastructural features of the clusters (figure 24). The vesicular membranes and the electron density surrounding them are identifiable and can be used for correlation with the LM acquisition.

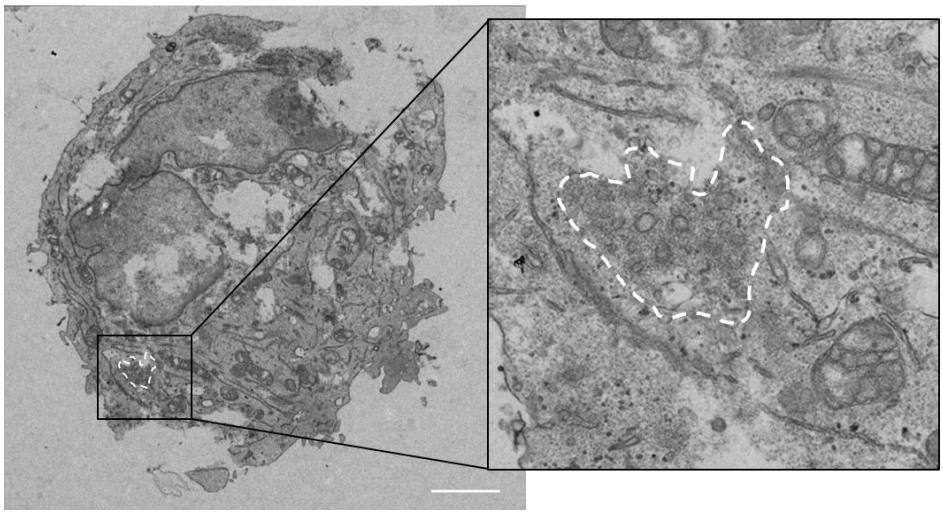

Figure 24. Ultrastructural preservation of an IAV 8 hours infected cell after FISH labeling and STORM acquisition

The damages in the ultrastructure are visible in an IAV 8 hours infected cell after FISH labelling and STORM acquisition, particularly in the extreme cytoplasmic extraction. Nevertheless, the vesicular clusters (white dashed line) are still identifiable. Bar = 2 µm. Images acquired on a Hitachi H-7650 operating at 100 keV and analysed by the software Fiji.

5.2.4.3 CLEM

Finally, the techniques FISH, LM, STORM and EM were joined to perform a complete CLEM assay (figure 25). First, FISH was performed as described in the section 4.5.5.1. FISH on Cryostat Sections for STORM. Next, cells of interest were acquired by LM and STORM at a high magnification to image cellular details and low magnification to record the carved grid pattern in the coverslip (figure 25A). The region of interest (ROI) where the cell is located, position P9, was recorded for further targeted ultramicrotomy.

Cells were subsequently processed for EM. After curing of the resin block, the coverslip with the grid was released from the surface of the block and the carved pattern and ROI could be easily located (figure 25B). This ROI was trimmed in a trapezoid shape (represented in white in the figure 25B) and sectioned for TEM. Both images from the trimmed resin block and ROI were merged to precisely identify the cell localization (yellow box, figure 25C). A low magnification image was acquired by

TEM and, once again, merged with the resin block picture for a confirmation of the cellular identification at the TEM level (figure 25D).

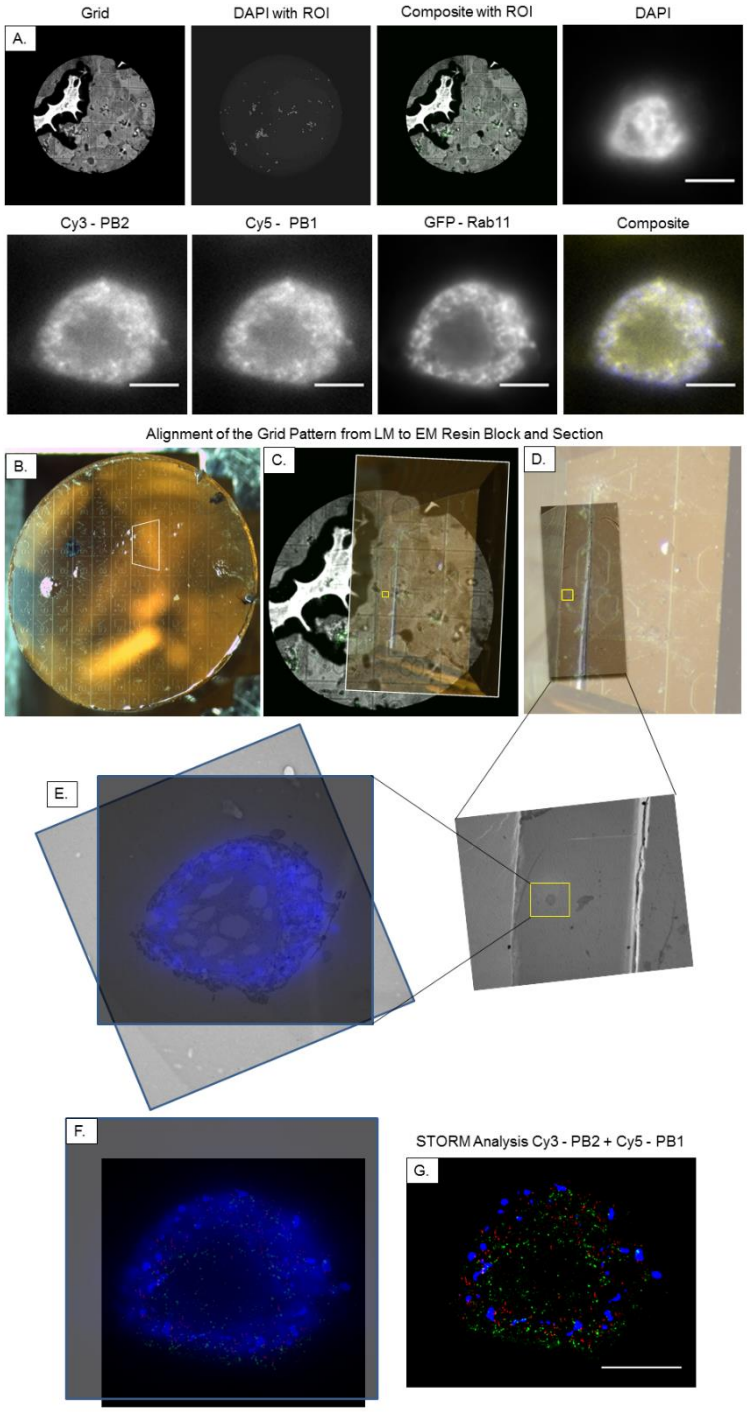

Figure 25. CLEM workflow for an IAV infected cell

Scheme of the developed CLEM method that combined FISH, LM, STORM and EM. **A.** LM images were acquired of the cell of interest and the ROI. **B.** After EM processing the ROI was trimmed and sectioned. **C.** To confirm the presence of the cell of interest an alignment was made between the resin block and the LM ROI image. **D.** the same alignment was done to correlate the cell in the resin block and the ultra-thin section. **E.** Several TEM images were acquired and lined up with the LM images. **F.** Finally the LM data was aligned with the STORM reconstruction. Bar = 5 µm. LM images acquired on a Nikon ECLIPSE TI, using a 100x 1.45 numerical aperture oil immersion objective. The STORM acquisition with the red laser Cy5 was done at 110 mW and with the green Cy3 at 80 mW with an exposure time of 10 ms in 20,000 images. EM images were acquired on a Hitachi H-7650 operating at 100 keV. All images were analysed by the Fiji software.

Several TEM images were acquired and later aligned with the pre-existent GFP-Rab11 image (represented in blue, figure 25E). The alignments do not fit entirely due to shape alterations induced by the EM processing after LM acquisition. The same alignments were done between the GFP-Rab11 image and the STORM reconstruction (figure 25F).

To correlate the viral segments with the ultrastructure associated, the STORM reconstruction was aligned with the TEM image (figure 26).

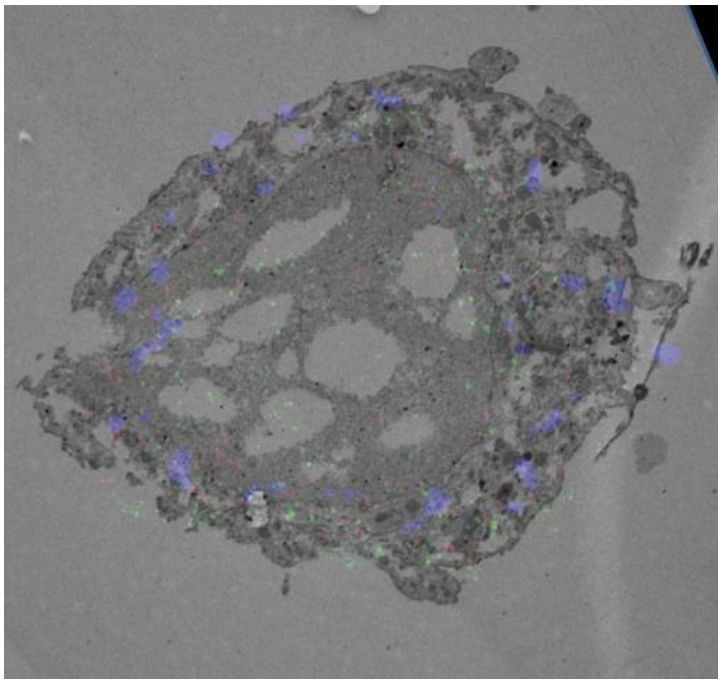

Figure 26. STORM reconstruction and EM alignment

Final alignment between the STORM reconstruction and the EM image. Poor correlation was achieved, with low precision. LM Images acquired on a Nikon ECLIPSE TI, using a 100x 1.45 numerical aperture oil immersion objective. The STORM acquisition with the red laser Cy5 was done at 110 mW and with the green Cy3 at 80 mW with an exposure time of 10ms in 20,000 images. EM images were acquired on a Hitachi H-7650 operating at 100 keV. All images were analysed by the software Fiji.

This final alignment was a challenge. The precision of the correlation was low, with several GFP-Rab11 fluorescent spots located outside the cellular perimeter and that did not match areas of vRNP labeling. For reaching more meaningful insights than already published, this CLEM methodology requires further troubleshooting, that, as observed, is not devoid of many obstacles.

6. Discussion

"The constant dilemma: on one hand to retain biological activity and on the other, to obtain good morphological preservation" – David Hopwood

6.1 Characterization of Vesicular Structures Induced by IAV Infection

Previous work showed that IAV infection induces aggregation of Rab11 vesicles, forming clusters by a mechanism that involves impairment of the flow of ERC vesicles to the surface. Within these clusters, heterogeneous vesicles of single and double membranes have been identified by ultrastructural analysis (Vale-Costa et al. 2016). This allowed the proposal of a model for the assembly of IAV genome in which clustered vesicles favored the formation of the RNA-RNA interactions required for genome assembly (figure 27A).

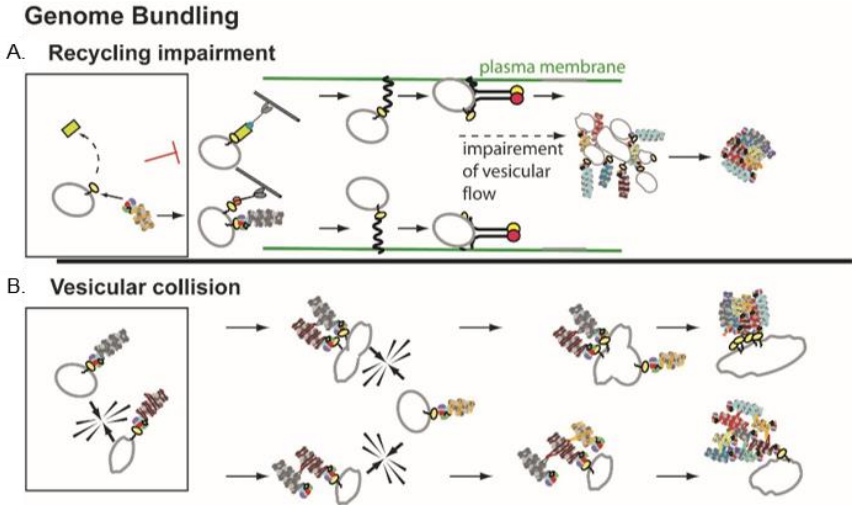

Figure 27. IAV genome bundling models

Two models were proposed for IAV genome bundling. **A.** In the Recycling impairment model, IAV infection induces the impairment of the flow of Rab11 vesicles from the ERC towards the plasma membrane. These vesicles aggregate in the cytoplasm creating clusters that favours the RNA-RNA interactions between the different segments necessary for genome assembly. In this model, genome assembly occurs downstream clustering. **B.** In the vesicular collision model, genome assembly occurs *en route* to the plasma membrane. The Rab11 vesicles transporting vRNPs collide with each other and fuse, leading to formation of a complete genomic set. Image produced by Maria João Amorim.

The recycling impairment model contrasts with a recent hypothesis, in which genome formation occurred while vRNPs were being transported to the plasma membrane through vesicular collision (figure 27B). The latter model, vesicular collision, was supported by experiments using super-resolution to analise two to four vRNPs. It was observed that the co-localization between distinct vRNPs increased as infection progressed in a Rab11 dependent manner.

Both models are based in changes undergone by Rab11 (as a result of infection), and inclusion of vRNPs in Rab11 occupied areas. Super-resolution methods have lower resolving power when compared to electron microscopy based approaches and both lack the resolution to resolve vRNPs and determine if vRNPs are individually bound to Rab11 vesicles or in a complex.

To validate our model we set out experiments to determine the composition of clustered vesicles in terms of 1) numbers of SMV and DMV; 2) Rab11 and vRNPs and 3) cellular environment of these vesicles. For these goals, a series of methodologies were developed, and applied to the study of IAV infected cells.

6.1.1 High Pressure Freezing – Freeze Substitution Optimization: Vitrification and Morphological Preservation

Both vitrification and morphological preservation were evaluated during optimization of the HPF-FS EM-cryo technique. The best vitrification rate was achieved with aluminum hats combined with dextran as a cryo-protectant (figure 11). These result can be justified by the excellent thermal conductivity of aluminum in comparison to aclar and by the ability of dextran, a high-molecular weight polysaccharide, to form a rich shell around the crystals that inhibit their growth (Jimenez et al. 2006; Yakovlev & Downing 2011).

Conversely, aclar flat disks – chosen amongst those with good vitrification – led to a better preservation of the ultrastructure (figure 12) compared to hats. A possible explanation is the fact that sample handling is physically demanding in hats, but reduced to a minimum in flat disks. Aluminum hats imply pelleting and centrifugation of cells, whereas in flat disks all the steps are made *in situ*. Formation of ice crystals smaller than the resolution cannot be excluded here, but if they are present, they did not impact the ultrastructure preservation since no empty spaces or clumping of ribosomes was visible and the vesicular membranes appeared preserved.

Additionally, the filler dextran can also contribute to the poor morphologic preservation of hats. On one hand, the shell of dextran prevents the growth of ice crystals, but on the other hand it binds to uranium and tannic acid therefore hindering solvent exchange during FS. The created barrier prevents the proper substitution of water for solvents and leads to an inferior preservation of ultrastructure (Giddings 2003; Jimenez et al. 2006).

The superior morphological preservation obtained with flat disks could be confirmed through a set of quantitative criteria to evaluate ultrastructural morphology maintenance (figure 12). The flat disks obtained median score of 77.8% when compared to the 55.6% obtained by the hats.

In summary, aclar flat disks were the best specimen carrier to perform HPF-FS for the characterization of the ultrastructure of vesicular clusters in IAV-infected cells.

6.1.2 Quantification of Vesicle Number during IAV Infection

The number of SMVs and DMVs was counted during an IAV time-course infection to study the progression of vesicles (figure 14 and 15, respectively). At the early IAV infection time-point of 4 hours no virus-specific modification of SMVs number was detected. The small number of SMV counted showed no differences when compared to uninfected cells, which work as a control. This result shows a correlation between the number of SMVs and the trafficking of vRNPs, since IAV vRNPs are just exported from the nucleus at this time-point and there is not yet movement towards the cell periphery.

High numbers of SMVs (in clusters) were detected from 8 hours IAV PI until the last quantified infection time-point of 24 hours. From 8 hours PI until later infection time-point of 20 hours there is a

constant release of virus. After 20 hours, the number of released particles decrease but there is still trafficking of viral components towards the plasma membrane (Frensing et al. 2016). This can justify the high and constant numbers of SMVs detected and their usage as trafficking vehicles of vRNPs and potentially for platforms for genome assembly.

The DMVs quantification showed that these vesicles are induced by IAV infection, and are formed after vRNPs nuclear export, but their numbers are very low. In mock cells and in 4 hours infected cells, no DMVs were found which support the absence of these structures in homeostasis but also, before vRNPs trafficking in infection. These results are intriguing, since DMVs were only described in positive sense RNA virus where replication is made in membranous replication factories induced by the virus (Blanchard & Roingeard 2015).

6.1.3 3D Morphological Study

A tomographic and 3D study was done, to further investigate the cellular ultrastructural context and the biogenesis of the vesicular structures detected (figure 17 and 18, respectively). It was detected a close relation between DMVs, SMVs and ER at 16 hours IAV PI, which can suggest that the ER might be involved in the formation of vesicular clusters. This result needs further investigation in early infection time-points, to detect the initial structural dynamics.

In positive-sense RNA virus the membranous replication factories can evolve from ER or endosomes membrane re-arrangements (Blanchard & Roingeard 2015). Taking into account that IAV replication occurs within the cellular nucleus, this observation proposes that the ER relation with the vesicles can be connected not with replication but to the later steps of trafficking and assembly. Also, as in the positive-sense RNA virus it can be related with protection of the viral genome and proteins from the host cytoplasmic immune sensors which suggest that non-closely related virus may share the same or similar pathways in the cell.

6.2 Clustered Structures Origin and Cellular Context

To determine the cellular context in the vicinity of clustered vesicles, immuno-gold labeling was performed with markers for ER, ERC, Golgi and viral genome. However, due to the susceptibility of antigens to fixation, an optimization was initially done.

6.2.1 Immunolabeling Optimization

Fixation conditions were optimized by LM to maintain the equilibrium between ultrastructure and immunoreactivity preservation. Three aldehydes mixtures of 2% FA with 0.2, 0.1 and 0.05% of GA and the control fixative 4% FA were tested (figure 19).

The best fixative was 4% FA permitted the labelling of all four markers. This result can be explained by the lower cross-linking capability and epitope alteration of FA when compared with GA (Bancroft & Gamble 2002). Although, fixatives with GA contribute to an enhanced ultrastructural preservation, the fixative chosen allows the labelling of all the markers needed which was the main goal to define the origin of the vesicles within the clusters.

6.2.2 Electron Microscopy Analysis

The vesicular clustering we demonstrated for IAV infection lacked labeling of membranes and vRNPs to precisely match membrane type with vRNP carriers. DMV are hallmarks of infection by many positive-sense RNA viruses, *e.g.* Picornaviruses, but in IAV infection were never described and could be a byproduct of infection unrelated with vRNP transport. The analyses of the labeling allowed defining that both SMVs and DMVs are related with the ERC and are involved in the trafficking of IAV viral genome (because Rab11 and NP were found in DMV). Moreover, it confirms that with the current resolving power, we are unable to state that complete assembled IAV genomes are found in clustered vesicles. Hence, our model in which vRNPs hotspots are created for the establishment of interactions between the segments and assembly of a complete genome set is valid and requires testing.

6.3 CLEM Method Development

A CLEM method that gathers FISH in cryostat sections, STORM and EM techniques was developed and tested within this work to further investigate the functionality of DMVs in IAV vRNPs transport and genomic assembly. Several optimizations were done within each technique to achieve the combined CLEM method.

First, in the FISH on cryostat sections, it was established that the support that gave the best results was coverslips coated with 2% APES. The coverslip permitted the LM imaging, is resistant and non-reactive with the EM chemicals and holds the section during all the procedures when coating is added due to an increased adherence. The coverslip was easily released from the resin block when comparing to the glass slide. The glass slide easily breaks leaving traces of glass in the resin and this can be due to the glass thickness difference.

In the present form STORM acquisitions of distinct vRNPs by FISH are not conclusive (figure 23). It was detected a correspondence between the segments and the clusters of Rab11 by LM but not in the STORM reconstructed images. In the EM technique part, both vesicles were still recognizable, although the preservation of cellular ultrastructure suffered a lot of damage, extraction and shape modifications (figure 24).

Hence, the STORM reconstructions from cells aligned with LM and EM images resulted in no correlation between vRNPs, Rab11 and clustered vesicles with this method. Considerable advances will be required for the development of the CLEM technique. Current limitations of the resolving power by LM and EM microscopy impede the resolution of the genomic content transported by each vesicle.

7. Conclusion

"Those who have cautiously done no more than they believed possible, have never taken a single step forward" – Mikhail Bakunin

It is well accepted that IAV genome assembly is maintained by RNA-RNA interactions (Hutchinson et al 2010). Fundamental studies imaged fully assembled IAV genomes budding at the plasma membrane (Fournier et al. 2012; Noda et al. 2012). However, the precise cellular location where genome assembly takes place remains unclear. Recent manuscripts suggest that genome assembly occurs gradually as ERC vesicles carrying vRNPs (facing the cytosol) collide *en route* to the plasma membrane (Lakdawala et al. 2014; Chou et al. 2013). Two mechanisms were proposed both related with vesicular collision (figure 28).

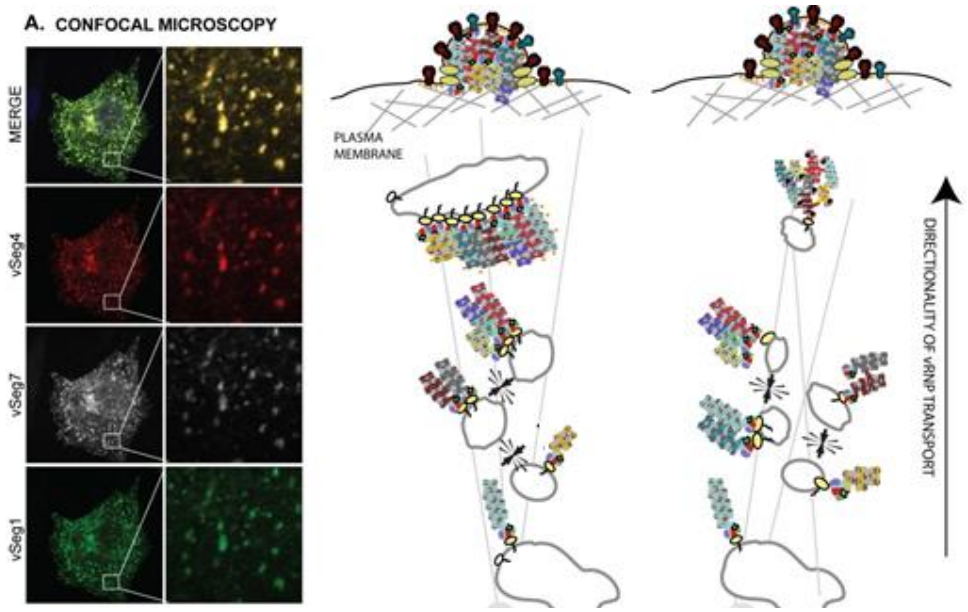

Figure 28. Vesicular collision models

Super-resolution and confocal microscopy analysis during IAV infection led to the observation that the 8 vRNPs core that constitute a virion, started co-localizing as progeny vRNPs were transported to the plasma membrane. This co-localization was dependent on Rab11. The observations stated led to the proposal of vesicular collision models in which the 8-segment core to be included in a virion was formed during the transport. Image produced by Maria João Amorim.

Though, recently the Amorim group showed that while being transported on ERC vesicles, vRNPs competed with some cellular factors and inhibited the normal flow of the ERC vesicles leading to clustering. Such mechanism offers an alternative solution to IAV genomic assembly, whereby clustering originates hotspots containing all vRNP types for posterior assembly (Vale-Costa et al. 2016) (figure 29).

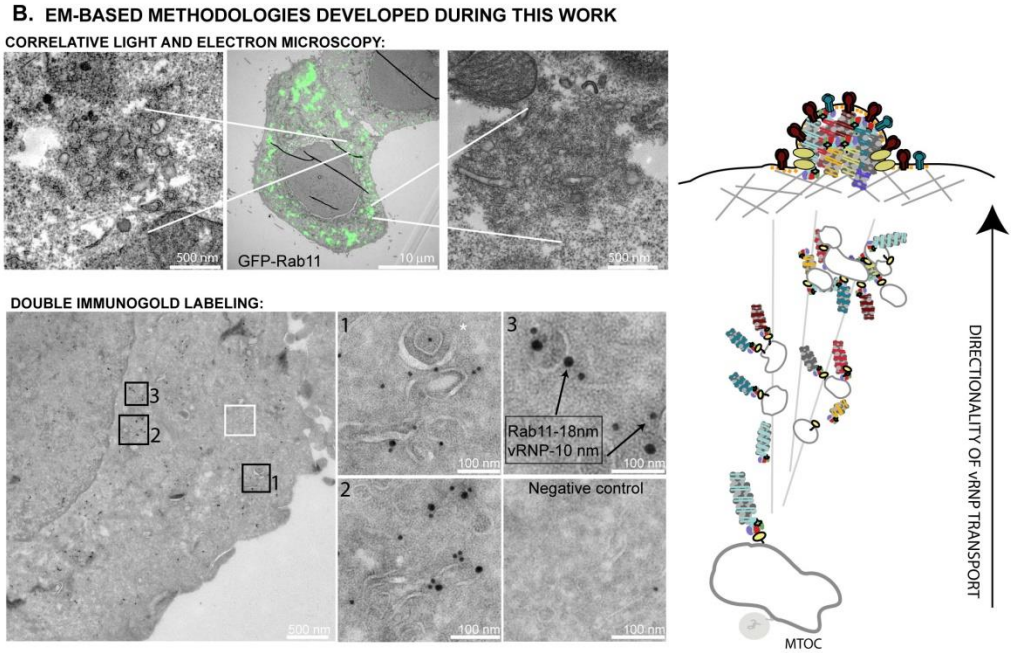

Figure 29. Recycling impairment model

EM-based approaches in IAV infected cells led to the observation that the 8 vRNPs core that constitute a virion concentrate in clustered vesicles, formed in a Rab11 dependent manner. This observations suggests that genome assembly could operate downstream the formation of clustered vesicles. Image produced by Maria João Amorim.

This work was done to test both model hypotheses. It was shown that the number of clustered SMVs - used as vehicles for vRNP trafficking - increased during IAV infection whilst the number of DMVs remained very low. Perhaps, the most relevant findings of this work relate with the immunogold labelling staining of Rab11 and vRNPs in these clusters that confirmed that both carry vRNPs. Hence, Rab11 positive SMVs (in their majority) and DMVs (in reduced numbers) constitute the clusters formed during infection that we propose to operate as platforms for spatial convergence of vRNPs.

Nevertheless, a third hypothesis needs to be considered that is a combination of both models. Partial genome assembly via vesicular collision could also facilitate clustering of Rab11 vesicles (creating an environment that could facilitate its completion) (Vale-Costa et al. 2016). Intriguingly, studies employing high resolution electron microscopy found no clear evidence of supramolecular complexes in the areas of clustered vesicles (Vale-Costa et al. 2016), but it is very likely that the resolution required for such claim has not been attained.

All these studies highlight the fact that the assembly of IAV genome is far from understood. Fascinating outstanding questions that await clarification include: do vRNPs reach the budding sites at the plasma membrane as a sort of supramolecular complex (sub-bundle or complete genome)?; Does vesicular clustering contribute to viral assembly?; What are the molecular mechanisms leading to vesicular clustering?; Is Rab11 the final carrier of vRNP-containing vesicles to the plasma membrane?; and finally, what other means does the virus explore to transport vRNPs (and other viral proteins) to assembly sites?

7.1 Future Perspectives

The EM cryo-techniques optimized within the scope of this Master thesis are crucial to determine that within clustered vesicles, SMVs and DMVs, carry vRNPs but fail to answer if IAV genome assembly are done in these areas.

To resolve if IAV genome assembly precedes or follows vesicular clustering, other future experiments might be requiring using, for example, packaging mutants. These mutants are viruses that have a defect in specific segments to be incorporated in virions and differ from WT viruses in nucleic acid composition but not in viral protein function (Hutchinson et al 2010). We predict that if genome assembly takes place upstream clustering (in the colliding model), packaging mutants will localize less in clusters. Conversely, if clustered vesicles constitute sites of vRNP concentration for subsequent assembly, then the levels of packaging mutants and WT segments within these loci will be similar.

FISH, TEM and CLEM techniques will help to localize and do the stoichiometry of packaging mutants of all segments in clustered vesicles.

8. Appendix

8.1 Appendix 1 – Publications Resulting from Work Carried Out during my Masters

1) **Sousa, A.L**; Vale-Costa, S; Amorim, M.J; Tranfield, E.M. Using correlative light and electron microscopy to understand influenza A viral assembly, Ultrastruct Pathol. 2017.

   I performed the electron microscopy work and co-wrote this manuscript with Dr Erin Tranfield.

2) Vale-Costa, S; Alenquer, M; **Sousa, A.L**; Kellen, B; Ramalho, J; Tranfield, E.M; Amorim, M.J. Influenza A virus ribonucleoproteins modulate host recycling by competing with Rab11 effectors, J Cell Sci. 2016.

   I performed the electron microscopy work and contributed to the light microscopy work inserted in the correlative light electron microscopy technique (CLEM) used for observation of clustering of vesicles which helped to elucidate IAV assembly.

8.2 Appendix 2 – Conferences and Courses Attended during my Masters

1) July, 2017 - Speaker at Microscience Microscopy Congress (Manchester, United Kingdom) – "All for One and One for All: A Multi-Methodology Approach to the Study of Influenza A Virus at the Nanoscale".

2) April, 2016 – Trainee at EMBL Course: High-Accuracy Correlated Light and Electron Microscopy: Application at Room Temperature and in Cryo. European Molecular Biology Laboratory (Heidelberg, Germany).

9. References

Acheson, N.H., 2011. *Fundamentals of Molecular Virology*, John Wiley & Sons, Inc.

Akkina, R.K., 1990. Antigenic reactivity and electrophoretic migrational heterogeneity of the three polymerase proteins of type A human and animal influenza viruses. *Archives of Virology*, 111(3–4), pp.187–197.

Amorim, M.J. et al., 2011. A Rab11- and microtubule-dependent mechanism for cytoplasmic transport of influenza A virus viral RNA. *Journal of virology*, 85(9), pp.4143–56.

Arranz, R. et al., 2012. The Structure of Native Influenza Virion Ribonucleoproteins. *Science*, 338(6114), pp.1634–1637.

Bancroft, J.D. & Gamble, M., 2002. *Theory and Practice of Histological Techniques* Fifth edit. J. D. Bancroft & M. Gamble, eds., Harcourt Publishers.

Blanchard, E. & Roingeard, P., 2015. Virus-induced double-membrane vesicles. *Cellular Microbiology*, 17(1), pp.45–50.

Bouvier, N.M. & Palese, P., 2008. The biology of influenza viruses. *Vaccine*, 26(SUPPL. 4).

Braakman, I. et al., 1991. Folding of influenza hemagglutinin in the endoplasmic reticulum. *Journal of Cell Biology*, 114(3), pp.401–411.

Braam, J., Ulmanen, I. & Krug, R.M., 1983. Molecular model of a eucaryotic transcription complex: Functions and movements of influenza P proteins during capped RNA-primed transcription. *Cell*, 34(2), pp.611–618.

Bui, M. et al., 2000. Role of the influenza virus M1 protein in nuclear export of viral ribonucleoproteins. *Journal of virology*, 74(4), pp.1781–6.

Chen, W. et al., 2001. A novel influenza A virus mitochondrial protein that induces cell death. *Nature Medicine*, 7(12), pp.1306–1312.

Chou, Y. ying et al., 2013. Colocalization of Different Influenza Viral RNA Segments in the Cytoplasm before Viral Budding as Shown by Single-molecule Sensitivity FISH Analysis. *PLoS Pathogens*, 9(5).

Compans, R.W. et al., 1970. Influenza virus proteins. I. Analysis of polypeptides of the virion and identification of spike glycoproteins. *Virology*, 42(4), pp.880–889.

Connor, R.J. et al., 1994. Receptor specificity in human, avian, and equine H2 and H3 influenza virus isolates. *Virology*, 205(1), pp.17–23.

Dias, A. et al., 2009. The cap-snatching endonuclease of influenza virus polymerase resides in the PA subunit. *Nature*, 458(7240), pp.914–918.

Eisfeld, A.J. et al., 2011. RAB11A Is Essential for Transport of the Influenza Virus Genome to the Plasma Membrane. *Journal of Virology*, 85(13), pp.6117–6126.

Fields, B.N., Knipe, D.M. & Howley, P.M., 2007. *Fields Virology, 5th Edition*.

Fournier, E. et al., 2012. A supramolecular assembly formed by influenza A virus genomic RNA segments. *Nucleic Acids Research*, 40(5), pp.2197–2209.

Frensing, T. et al., 2016. Influenza virus intracellular replication dynamics, release kinetics, and particle morphology during propagation in MDCK cells. *Applied Microbiology and Biotechnology*, 100(16), pp.7181–7192.

Giddings, T.H., 2003. Freeze-substitution protocols for improved visualization of membranes in high-pressure frozen samples. *Journal of Microscopy*, 212(1), pp.53–61.

Giese, S., Bolte, H. & Schwemmle, M., 2016. The feat of packaging eight unique genome segments. *Viruses*, 8(6).

Grant, B.D. & Donaldson, J.G., 2009. Pathways and mechanisms of endocytotic recycling. *Molecular Cell Biology*, 10(9), pp.597–604.

Griffiths, G., 1993. *Fine Structure Immunocytochemistry*, Trends in Cell Biology. doi:10.1007/978-3-642-77095-1.

Hause, B. et al., 2014. Characterization of a novel influenza virus strain in cattle and swine: proposal for a new genus in the Orthomyxoviridae family. *MBio*, 5(2), pp.1–10.

Hause, B.M. et al., 2013. Isolation of a Novel Swine Influenza Virus from Oklahoma in 2011 Which Is Distantly Related to Human Influenza C Viruses. *PLoS Pathogens*, 9(2).

Holsinger, L.J. et al., 1994. Influenza A Virus M2 Ion Channel Protein : a Structure-Function Analysis. , 68(3), pp.1551–1563.

Hutchinson, E.C. et al., 2014. Conserved and host-specific features of influenza virion architecture. *Nature Communications*, 5, p.4816.

Hutchinson, E.C. et al., 2010. Genome packaging in influenza A virus. *Journal of General Virology*, 91(2), pp.313–328.

Jagger, B.W. et al., 2012. An Overlapping Protein-Coding Region in Influenza A Virus Segment 3 Modulates the Host Response. *Science*, 337(6091), pp.199–204.

Jimenez, N. et al., 2006. Aclar discs: A versatile substrate for routine high-pressure freezing of mammalian cell monolayers. *Journal of Microscopy*, 221(3), pp.216–223.

Kemler, I., Whittaker, G. & Helenius, A., 1994. Nuclear Import of Microinjected Influenza Virus Ribonucleoproteins. *Virology*, 202(2), pp.1028–1033.

Kremer, J.R., Mastronarde, D.N. & McIntosh, J.R., 1996. Computer visualization of three-dimensional image data using IMOD. *Journal of structural biology*, 116(1), pp.71–6.

Lakdawala, S.S. et al., 2014. Influenza A Virus Assembly Intermediates Fuse in the Cytoplasm. *PLoS Pathogens*, 10(3).

Lamb, Robert and Choppin, P., 1983. The Gene Structure. *Ann. Rev. Biochem.*, pp.467–506.

Lee, N. et al., 2017. Genome-wide analysis of influenza viral RNA and nucleoprotein association. *Nucleic Acids Research*, 45(15), pp.8968–8977.

Lofgren, E. et al., 2007. Influenza seasonality: underlying causes and modeling theories. *Journal of virology*, 81(11), pp.5429–5436.

Maddox, P.H. & Jenkins, D., 1987. 3-Aminopropyltriethoxysilane (APES): a new advance in section adhesion. *Journal of clinical pathology*, 40(10), pp.1256–7.

Mastronarde, D.N., 1997. Dual-Axis Tomography: An Approach with Alignment Methods That Preserve Resolution. *Journal of Structural Biology*, 120(3), pp.343–352.

Matlin, K.S. et al., 1981. Infectious entry pathway of influenza virus in a canine kidney cell line. *Journal of Cell Biology*, 91(3 I), pp.601–613.

Matrosovich, M.N. et al., 2004. Neuraminidase is important for the initiation of influenza virus infection in human airway epithelium. *J Virol*, 78(22), pp.12665–12667.

McDonald, K., 2007. Cryopreparation Methods for Electron Microscopy of Selected Model Systems. *Methods in Cell Biology*, 2007(79), pp.23–56.

McGeoch, D., Fellner, P. & Newton, C., 1976. Influenza virus genome consists of eight distinct RNA species. *Proceedings of the National Academy of Sciences of the United States of America*, 73(9), pp.3045–9.

Mobius, W., 2009. Cryopreparation of biological specimens for immunoelectron microscopy. *Annals of Anatomy*, 191(3), pp.231–247.

Moeller, A. et al., 2012. Organization of the Influenza Virus Replication Machinery. *Science*, 338(6114), pp.1631–1634.

Momose, F. et al., 2011. Apical transport of influenza A virus ribonucleoprotein requires Rab11-positive recycling endosome. *PLoS ONE*, 6(6).

Moor, H., 1987. Theory and Practice of High Pressure Freezing. In *Cryotechniques in biological electron microscopy*. pp. 175–191.

Morphew, M.K., 2000. *Practical Methods in High-Pressure Freezing, Freeze-Substitution, Embedding and Immunocytochemistry for Electron Microscopy*, Boulder, Colorado: Laboratory for 3-D Fine Structure - Dept. of MCD Biology - University of Colorado.

Mosley, V.M. & Wyckoff, R.W.G., 1946. Electron Micrography of the Virus of Influenza. *Nature*.

Neumann, G., Castrucci, M.R. & Kawaoka, Y., 1997. Nuclear import and export of influenza virus nucleoprotein. *Journal of virology*, 71(12), pp.9690–700.

Noda, T. et al., 2012. Three-dimensional analysis of ribonucleoprotein complexes in influenza A virus. *Nature Communications*, 3, p.639.

O'Neill, R.E. et al., 1995. Nuclear import of influenza virus RNA can be mediated by viral nucleoprotein and transport factors required for protein import. *Journal of Biological Chemistry*, 270(39), pp.22701–22704.

O'Neill, R.E., Talon, J. & Palese, P., 1998. The influenza virus NEP (NS2 protein) mediates the nuclear export of viral ribonucleoproteins. *EMBO Journal*, 17(1), pp.288–296.

Palese, P. & Schulman, J.L., 1976. Mapping of the influenza virus genome: identification of the hemagglutinin and the neuraminidase genes. *Proceedings of the National Academy of Sciences of the United States of America*, 73(6), pp.2142–6.

Pasqualato, S. et al., 2004. The Structural GDP/GTP Cycle of Rab11 Reveals a Novel Interface Involved in the Dynamics of Recycling Endosomes. *Journal of Biological Chemistry*, 279(12), pp.11480–11488.

Peng, Q. et al., 1996. Influenza A virus RNA-dependent RNA polymerase cleaves influenza mRNA in vitro. *Virus Research*, 42(1–2), pp.149–158.

Pielak, R.M. & Chou, J.J., 2011. Influenza M2 proton channels. *Biochimica et Biophysica Acta - Biomembranes*, 1808(2), pp.522–529.

Ritchey, M.B., Palese, P. & Schulman, J.L., 1976. Mapping of the influenza virus genome. III. Identification of genes coding for nucleoprotein, membrane protein, and nonstructural protein. *Journal of virology*, 20(1), pp.307–13.

Robertson, J.S., Schubert, M. & Lazzarini, R.A., 1981. Polyadenylation sites for influenza virus mRNA. *Journal of virology*, 38(1), pp.157–63.

Rodriguez-Boulan, E. et al., 1984. Intracellular transport of influenza virus hemagglutinin to the apical surface of Madin-Darby canine kidney cells. *The Journal of cell biology*, 98(1), pp.308–319.

Roingeard, P., 2008. Viral detection by electron microscopy: past, present and future. *Biology of the cell / under the auspices of the European Cell Biology Organization*, 100(8), pp.491–501.

Romero-Brey, I. & Bartenschlager, R., 2015. Viral infection at high magnification: 3D electron microscopy methods to analyze the architecture of infected cells. *Viruses*, 7(12), pp.6316–6345.

Rossman, J.S. et al., 2010. Influenza Virus M2 Protein Mediates ESCRT-Independent Membrane Scission. *Cell*, 142(6), pp.902–913.

Rossmann, M.G., Rao, V.B. (Eds), 2012. *Viral Molecular Machines.* Springer US, Boston, MA.

doi:10.1007/978-1-4614-0980-9.

Rust, M.J. et al., 2004. Assembly of endocytic machinery around individual influenza viruses during viral entry. *Nature Structural & Molecular Biology*, 11(6), pp.567–573.

Rust, M.J., Bates, M. & Zhuang, X., 2006. Stochastic optical reconstruction miscroscopy (STORM) provides sub-diffraction-limit image resolution. *Nat. Methods*, 3(10), pp.793–795.

Saunders-Hastings, P. & Krewski, D., 2016. Reviewing the History of Pandemic Influenza: Understanding Patterns of Emergence and Transmission. *Pathogens*, 5(4), p.66.

Selman, M. et al., 2012. Adaptive mutation in influenza A virus non-structural gene is linked to host switching and induces a novel protein by alternative splicing. *Emerging Microbes & Infections*, 1(11), p.e42.

Skehel, J.J. & Wiley, D.C., 2000. Receptor binding and membrane fusion in virus entry: the influenza hemagglutinin. *Annual review of biochemistry*, 69, pp.531–69.

Studer, D., Michel, M. & Muller, M., 1989. High-Pressure Freezing Comes Of Age. *Scanning Microscopy*, (Suppl. 3), pp.253–269.

Takahashi, S. et al., 2012. Rab11 regulates exocytosis of recycling vesicles at the plasma membrane. *Journal of cell science*, 125(Pt 17), pp.4049–57.

Taubenberger, J.K. & Kash, J.C., 2010. Influenza virus evolution, host adaptation, and pandemic formation. *Cell Host and Microbe*, 7(6), pp.440–451.

Tokuyasu, K.T., 1973. A technique for ultracryotomy of cell suspensions and tissues. *Journal of Cell Biology*, 57(2), pp.551–565.

Tong, S. et al., 2013. New World Bats Harbor Diverse Influenza A Viruses. *PLoS Pathogens*, 9(10).

Ulmanen, I., Broni, B.A. & Krug, R.M., 1981. Role of two of the influenza virus core P proteins in recognizing cap 1 structures (m7GpppNm) on RNAs and in initiating viral RNA transcription. *Proceedings of the National Academy of Sciences of the United States of America*, 78(12), pp.7355–9.

Vale-Costa, S. et al., 2016. Influenza A virus ribonucleoproteins modulate host recycling by competing with Rab11 effectors. *J Cell Sci*, pp.1697–1710.

Vale-Costa, S. & Amorim, M.J., 2016. Recycling endosomes and viral infection. *Viruses*, 8(3), pp.6–10.

Varghese, J.N., Laver, W.G. & Colman, P.M.O., 1983. Structure of the influenza virus glycoprotein antigen neuraminidase at 2.9 Å resolution. *Nature*.

te Velthuis, A.J.W. & Fodor, E., 2016. Influenza virus RNA polymerase: insights into the mechanisms of viral RNA synthesis. *Nature Reviews Microbiology*, 14(8), pp.479–493.

Verkade, P. & Muller-Reichert, T., 2012. *Correlative Light and Electron Microscopy* 1st editio. P. Verkade & T. Muller-Reichert, eds.,

Vogels, I.M.C., Hoeben, K.A. & Van Noorden, C.J.F., 2009. Rapid combined light and electron microscopy on large frozen biological samples. *Journal of Microscopy*, 235(3), pp.252–258.

Wiley, D.C. & Skehel, J.J., 1987. The structure and function of the hemagglutinin membrane glycoprotein of influenza virus. *Structure*.

Wise, H.M. et al., 2009. A Complicated Message: Identification of a Novel PB1-Related Protein Translated from Influenza A Virus Segment 2 mRNA. *Journal of Virology*, 83(16), pp.8021–8031.

Wise, H.M. et al., 2012. Identification of a Novel Splice Variant Form of the Influenza A Virus M2 Ion Channel with an Antigenically Distinct Ectodomain. *PLoS Pathogens*, 8(11).

Yakovlev, S. & Downing, K.H., 2011. Freezing in sealed capillaries for preparation of frozen hydrated sections. *Journal of Microscopy*, 244(3), pp.235–247.

Yamayoshi, S. et al., 2014. Identification of a novel viral protein expressed from the PB2 segment of Influenza A Virus. *Journal of Virology*, 90(October), p.375.

Zheng, W. & Tao, Y.J., 2013. Structure and assembly of the influenza A virus ribonucleoprotein complex. *FEBS Letters*, 587(8), pp.1206–1214.